J. Fluid Mech. (1993), vol. 253, pp. 211–243

# An analytical study of transport in Stokes flows exhibiting large-scale chaos in the eccentric journal bearing

By TASSO J. KAPER[1]† AND S. WIGGINS[2]
[1] Division of Applied Mathematics, Brown University, Providence, RI 02912, USA
[2] Applied Mechanics, California Institute of Technology, Pasadena, CA 91125, USA

(Received 20 December 1991 and in revised form 2 February 1993)

In the present work, we apply new tools from the field of adiabatic dynamical systems theory to make quantitative predictions of various important mixing quantities in quasi-steady Stokes flows which possess slowly varying saddle stagnation points. Many of these quantities can be obtained before experiments or numerical simulations are performed using only knowledge of the streamlines in steady-state flows and the externally determined flow parameters. The location and size of the main region in which mixing occurs is determined to leading order by the slowly sweeping instantaneous stagnation streamlines. Tracer patches get stretched by an amount $O(1/\epsilon)$ during each period, and the average striation thickness of the patch decreases by a factor of $\epsilon$ in the same time. Also, the rate of stretching of material interfaces is bounded from below with an analytically obtained exponentially growing lower bound. Finally, the highly regular appearance of islands in quasi-steady Stokes' flows is explained using an extension of the KAM theory. As an example to illustrate these results, we study the transport of passive scalars in a low Reynolds number flow in the two-dimensional eccentric journal bearing when the angular velocities of the cylinders are slowly modulated, continuously and periodically in time, with frequency $\epsilon$. In contrast to the flows usually studied with dynamical systems, these slowly varying systems are singular perturbation (apparently far from integrable) problems exhibiting large-scale chaos, in which the non-integrability is due to the slow, continuous $O(1)$ modulation of the position of the saddle stagnation point and the two streamlines stagnating on it.

## 1. Introduction

Experimentally and numerically, it has been discovered that a patch of tracer fluid in a time-periodic Stokes flow rapidly develops into a highly striated lamellar structure as it gets stretched exponentially and folded, see Aref & Balachandar (1986), Chaiken *et al.* (1986, 1987), Chien, Rising & Ottino (1986), Leong & Ottino (1989), and Swanson & Ottino (1990). Although the flows in these studies are laminar, they simultaneously possess chaotic particle paths and large-scale structures, such as whorls, tendrils, periodic points, Smale horseshoes, and islands. To date, the tools used for extracting quantitative information about these flows have been *a posteriori*. For example, Lyapunov characteristic exponents have been computed for some of these flows with different geometries and mainly with stirring protocols of the 'blinking' type, where, to take the case of eccentric journal bearing flow, the two cylinders are

---

† Present address: Department of Mathematics, Boston University, Boston, MA 02215, USA.

rotated alternately in time in an on–off, or 'blinking', fashion. Using these *a posteriori* measures it is verified that nearby trajectories separate exponentially in time. In addition, it is typically found that a spatially non-uniform distribution exists for the finite-time measurements of stretch rates which depends in a nonlinear way on the flow parameters, see for example Muzzio, Ottino & Swanson (1991). Despite the fact that the empirical stretching rates obtained from these experimental and numerical techniques have been well-correlated with the flow parameters, no theory has been developed to date with the power to predict these rates before numerical or experimental simulations are performed.

The present work is also directed toward the goal of quantifying stretching and mixing. However, rather than rely on *a posteriori* measures, we develop for the first time a predictive theory for stretching and mixing quantities in quasi-steady Stokes flows exhibiting large, $O(1)$-sized chaotic regions.

We study transport of tracer particles in a low Reynolds number flow in a two-dimensional, counter-rotating eccentric journal bearing. This geometry, discussed in §2, is widely used in the study of mixing, see for example Aref & Balachandar (1986), Chaiken *et al.* (1986, 1987), Aref & Jones (1989), and Swanson & Ottino (1990). We show analytically that large-amplitude, continuous, slow, and periodic modulation of the angular velocities of the cylinders in time, as specified in §3, causes the integrable steady-state flow to exhibit large non-integrable regions. In contrast to the near-integrable (small-amplitude perturbations) flows usually studied with dynamical systems, however, these slowly varying systems are singular perturbation problems in which the non-integrability is due to the slow and continuous $O(1)$-amplitude modulation of the position of the saddle stagnation point and the two streamlines stagnating on it. Thus, they appear to be far from integrable.

In §4, an analytical technique is established to determine the location and size of the region in which mixing occurs, a region we call the mixing zone. The mixing zone is, to leading order, a large part of the $O(1)$-sized region swept out by the instantaneous separatrices during the modulation period. In §4, we also show that *a priori* control over the location and size of the mixing zone is possible using the three independent flow parameters: $\bar{e}$, the eccentricity of the bearing; $\Delta\bar{\Omega}$, the difference between the maximum and minimum of the ratio of the cylinder angular velocities; and $\epsilon$, the modulation frequency. As an example to illustrate this control, we determine the choice of parameters (within the context of our modulation protocols) for which the mixing zone occupies almost the entire fluid domain. Surprisingly, this combination consists of choosing $\bar{e}$ to be fairly small, so that the bearing is nearly concentric, $\Delta\bar{\Omega}$ to be large so that the instantaneous saddle stagnation point moves across most of the gap between the two cylinders, and $\epsilon$ to be moderately small, but not too small: $0.14 \leqslant \epsilon \leqslant 0.34$. Part of the theory in §4 relies on Arnol'd's extension of KAM theory to adiabatic dynamical systems. That the standard KAM theorem does not apply directly was previously recognized in Kaper & Wiggins (1989) and in Swanson & Ottino (1990).

In §5, a transport theory for the evolution of tracer particles in the mixing zone is developed using the slowly oscillating homoclinic tangle (the time-dependent analogue of the stagnation streamlines) as a template. As is well known in two-dimensional mixing studies, the mechanism governing transport across the tangle are the lobes formed by the segments of stable and unstable manifolds of the fixed points of the Poincaré map. However, the different structure of homoclinic tangles and lobes in adiabatic systems, as compared to all of the other flows – all near-integrable – to which these methods have been applied to date, requires special treatment. In particular, the shape of these lobes readily makes them identifiable as the mechanism by which the modulation causes the patches of tracer to develop into elaborately striated and folded lamellar structures. This refines the notion in the quasi-steady Stokes literature that tracer evolves along unstable manifolds. Finally in §5.4, we analytically derive exponentially growing lower bounds on the stretch rates for manifolds and tracer patches.

The results presented in §§4 and 5 are valid for a range of small $\epsilon$, but none, save one, are asymptotic results. In §6, we obtain $\epsilon \rightarrow 0$ asymptotic results using recently developed tools (see Kaper, Kovacic & Wiggins 1990; Kaper & Wiggins 1991*a*; and Elskens & Escande 1991) from the field of adiabatic dynamical systems. An adiabatic dynamical system is a Hamiltonian system which depends on a parameter (or a function) that varies slowly in time, but the size of the variation may be large. Adiabatic systems are singular perturbation problems, because of the presence of two asymptotically distinct timescales. The general form for time-dependent one-degree-of-freedom adiabatic dynamical systems is

$$\dot{q} = \frac{\partial H}{\partial p}(p,q;z), \quad \dot{p} = -\frac{\partial H}{\partial q}(p,q;z), \quad \dot{z} = \epsilon,$$

where $q$, $p$, and $z$ are scalars, $z$ is the slowly varying parameter, $H = H(q,p;z = \epsilon t)$ is the Hamiltonian, and $0 < \epsilon \ll 1$.

This theory gives asymptotic (as $\epsilon \rightarrow 0$) formulae valid for all times, including the short times of most interest in mixing, for the areas and lengths of lobes, for the average striation thickness of lamellar tracer patches (which constitutes a convective lengthscale), and for the rate of stretching of material interfaces. Lobe length increases by a factor of $O(1/\epsilon)$ during each period of the modulation, and the average striation thickness of a patch of tracer decreases by a factor of $O(\epsilon)$ every period. The ability to predict and control these quantities theoretically is important, and represents a step beyond the methods which rely on experimental data or the calculation of Lyapunov exponents. The theory also overcomes the limitations of dynamical systems tools that apply only to near-integrable systems, i.e. tools such as the usual Melnikov function (see Guckenheimer & Holmes 1983). Finally, the theory leads to a practical way in which our definition of the various mixing quantities, such as mixing zone, can be verified.

In §7, we explain theoretically for the first time the highly regular appearance of islands in quasi-steady Stokes flows, which contrasts with the behaviour of islands in regularly perturbed (near-integrable) flows. Adiabatic dynamical systems theory yields their location and states that their size is no bigger than $O(\epsilon)$, as $\epsilon \rightarrow 0$. In §8, we briefly discuss the precise sense in which these systems are chaotic. In §9, we discuss the robustness of our model by analysing the influence of the inertial terms. We also indicate how our results apply to other quasi-steady Stokes flows with slowly moving hyperbolic points, such as the two-roll mill, the cavity flow, and a geophysical flow, even when no analytical or numerical representation of the stream function is available. Finally, we present some results from numerical simulations which incorporate molecular diffusivity.

The difference between our modulation protocols and the 'stirring' protocols used in the literature may be summarized as follows. The protocols used in the literature prescribe the angular velocities of two cylinders $\Omega_1$ and $\Omega_2$, where the subscripts 1 and 2 refer to the casing and the shaft, respectively, either as a fairly rapid stirring:

$$\Omega_1(t) = \Omega_1 + \cos \omega t, \quad \Omega_2(t) = \Omega_2 - \cos \omega t,$$

where $\omega$ and $\Omega_i$ are $O(1)$, quantities for $i = 1, 2$, and $\Omega_1(t)\,\Omega_2(t) < 0$ for all $t$; or as a blinking modulation:

$$\Omega_1(t) = \begin{cases} \Omega_1, & 0 \leqslant t < \tfrac{1}{2}T \\ 0, & \tfrac{1}{2}T \leqslant t < T, \end{cases}$$

$$\Omega_2(t) = \begin{cases} 0, & 0 \leqslant t < \tfrac{1}{2}T \\ \Omega_2 & \tfrac{1}{2}T \leqslant t < T, \end{cases}$$

where $\Omega_1 \mp \Omega_2$, $\Omega_1\,\Omega_2 < 0$, and the period, $T$, is long compared to the characteristic time of the steady-state flow (Aref & Balachandar 1986; Swanson & Ottino 1990).

In contrast, the modulation protocols introduced in §3 prescribe a slow, large-amplitude modulation:

$$\Omega_1(\epsilon t) = \Omega_1 + \gamma \cos \epsilon t, \quad \Omega_2(\epsilon t) = \Omega_2 - \gamma \cos \epsilon t,$$

where $0 < \epsilon \ll 1$, $\gamma$ is a real constant of $O(1)$ magnitude, and $\Omega_2 < -\gamma < 0 < \gamma < \Omega_1$. The Strouhal number, an independent dimensionless parameter for these externally modulated flows (see Batchelor 1967, p. 216), satisfies $0 < Str \equiv \epsilon L/U \ll 1$, since the characteristic velocities and lengthscales in the flow $U$ and $L$ are $O(1)$ quantities independent of $\epsilon$.

The slow modulation protocols used throughout the present work are chosen so that tracer patches are already highly stretched and folded during the first few periods of the modulation, and so as to take advantage of the fact that the adiabatic dynamical systems tools we use are well-suited to the timescales of interest in mixing. All of the results reported in the present work are verified numerically for $\epsilon$ as large as 0.34.

The highly striated, thin lamellar structures in our simulations look similar to those obtained with blinking protocols. This is not surprising since the Fourier representation of the square-wave blinking protocol is an infinite series consisting of a sine function and all of its integral harmonics. Thus, the more harmonics added in our protocol with the correct amplitude, the closer one approximates the blinking protocol. Also, the underlying streamline (or topographical) map gets changed abruptly only every half-period in the blinking case whereas for our modulation protocols it is continuously being changed by tiny increments at each time step. For more discussion of the differences and similarities of blinking and non-blinking protocols, we refer the reader to Ottino (1989), Swanson (1991, chap. 5), and Swanson & Ottino (1990).

A visual comparison shows that after approximately two and a half modulation periods, the highly striated, thin lamellar structures observed in our simulations look similar, in terms of striation length and thickness and in terms of the number of folds, to those obtained in comparable geometries for blinking protocols after ten periods with $\theta = 630°$, see figure 2 in Swanson & Ottino (1990).

Because the modulation period is of length $2\pi/\epsilon$, the equations are stiff, and the numerics performed in this study for finding the fixed points of the Poincaré map and the manifolds are delicate. To integrate the equations, an implicit Gauss–Legendre symplectic fourth-order Runge–Kutta scheme was used. All numerical codes were tested on steady-state flows, reproducing the plots in Ballal & Rivlin (1976), and most computations were verified using a second symplectic integration scheme. Furthermore, for plotting the manifolds of the fixed point on the Poincaré map, we used a routine especially suited to adiabatic systems, see Kaper (1991, Part I, Appendix C). Finally, the hyperbolic periodic orbits of the full system in the extended phase space were obtained using the technique of multiple shooting, which yields uniformly valid representations of unstable orbits. We refer the reader to Kaper (1991, Part II) for the details of the numerical implementations.

Finally, the results presented in Kaper & Wiggins (1991*a*, *b*) and those in Elskens &

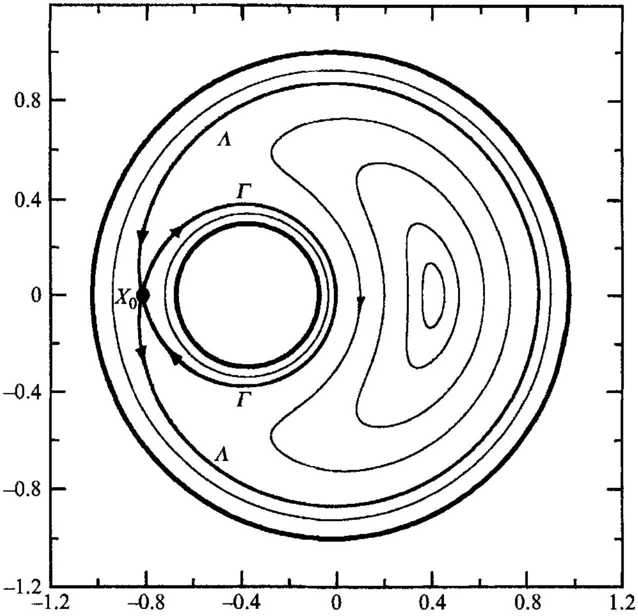

FIGURE 1. Steady-state counter-rotating eccentric journal bearing flow, with $\bar{e} = 0.5$, $R_1 = 1.0$, $R_2 = 0.3$, $\bar{r} = 0.3$ (where for Ballal & Rivlin $\xi_1 = -0.9397$, $\xi_2 = -1.9966$). The cylinders are the darkest circles. The inner circle rotates clockwise with $\Omega_2 = -4$, and the outer circle rotates counterclockwise with $\Omega_1 = 1$.

Escande (1991) also apply to adiabatic dynamical systems in which $H$ has more general dependence on $z$, including quasi-periodic and bounded non-periodic modulation. Thus, these results can be applied to the corresponding time-dependent modulation protocol to obtain quantitative information about stretching and transport in quasi-steady Stokes flows with more general time-dependence.

## 2. Steady counter-rotating flow

The integrable equations for the evolution of tracer particles in the steady flow are

$$\dot{x} = \frac{\partial \psi}{\partial y}(x, y; \Omega_1, \Omega_2), \quad \dot{y} = -\frac{\partial \psi}{\partial x}(x, y; \Omega_1, \Omega_2), \tag{2.1}$$

where $\psi$ is the stream function, $x$ and $y$ are the (canonically conjugate) Cartesian coordinates, and $\Omega_1$ and $\Omega_2$ are the angular velocities of the casing and the shaft, respectively. The stream function $\psi$ is linear in $\Omega_1$ and $\Omega_2$, and we have converted its bipolar coordinate representation obtained in Ballal & Rivlin (1976) to Cartesian coordinates. The Reynolds number is defined as

$$Re \equiv \frac{(R_1^2 \Omega_1^2 + R_2^2 \Omega_2^2)^{\frac{1}{2}} R_2}{\nu},$$

where $R_1$ and $R_2$ denote the radii of the casing and shaft, respectively, with $R_1 > R_2$, and $\nu$ is the kinematic viscosity. In using the results of Ballal & Rivlin (1976), we take $0 < Re \ll 1$, which is the limit of steady Stokes flow. Also, without loss of generality we take $R_1 = 1.0$.

The parameters for the steady flow are: $\bar{e} = \Delta x/(R_1 - R_2)$, the eccentricity of the bearing, where $\Delta x$ is the distance (measured in the same Cartesian coordinates shown

| $\bar{e}$ | $\bar{\Omega}$ | $A$ | $C$ | $B$ |
|---|---|---|---|---|
| 0.1 | −1 | 4.3 | 86.0 | 9.7 |
| 0.1 | −2 | 8.4 | 75.1 | 16.5 |
| 0.1 | −10 | 33.5 | 35.8 | 30.7 |
| 0.1 | −20 | 50.9 | 21.4 | 27.7 |
| 0.1 | −60 | 76.0 | 8.3 | 15.7 |
| 0.3 | −2 | 4.9 | 61.0 | 34.1 |
| 0.3 | −10 | 23.7 | 22.0 | 54.3 |
| 0.5 | −0.2 | 0.9 | 70.0 | 29.1 |
| 0.5 | −1 | 1.7 | 55.2 | 43.1 |
| 0.5 | −2 | 3.2 | 43.2 | 53.5 |
| 0.5 | −10 | 16.1 | 12.7 | 71.1 |
| 0.5 | −60 | 39.5 | 2.7 | 57.7 |
| 0.75 | −0.2 | 0.4 | 33.2 | 66.4 |
| 0.75 | −1 | 0.9 | 25.7 | 73.4 |
| 0.75 | −2 | 1.7 | 19.1 | 79.2 |
| 0.75 | −10 | 7.7 | 4.7 | 87.6 |
| 0.75 | −20 | 11.2 | 2.6 | 86.1 |
| 0.75 | −60 | 15.7 | 1.4 | 83.0 |

TABLE 1. Areas of the three regions in the steady-state flow domain as percentages of the total area inside the fluid domain and as a function of $\bar{e}$ and $\bar{\Omega}$. Column $A$ is for the region adjacent to the inner cylinder, $C$ for that adjacent to the outer cylinder, and $B$ is for the backflow region.

in the figures) between the centres of the cylinders; $\bar{\Omega} \equiv \Omega_2/\Omega_1$, the ratio of the angular velocities; and, $\bar{r} \equiv R_2/R_1$, the ratio of the radii of the cylinders. Our $\bar{e}$ and $\Delta x$ are identical to the variables $\bar{\epsilon}$ and $\epsilon$ in Ballal & Rivlin (1976, see §2 and equation (8.23)). Furthermore, for simplicity, the results we report in the present work are for the geometry with $\bar{r} = 0.3$. Simulations using other values of $\bar{r}$ are qualitatively similar to those obtained with this choice.

In the counter-rotating case ($\Omega_1 \Omega_2 < 0$), see figure 1, there is precisely one saddle stagnation point $X_0$ (hyperbolic fixed point) on the $x$-axis in the narrow gap for all values of $\bar{e}$, $\bar{r}$, $\Omega_1$ and $\Omega_2$, which is attached to itself by two stagnation streamlines (orbits homoclinic to the hyperbolic fixed point). These two stagnation streamlines, which are the inner and outer stagnation streamlines $\Gamma$ and $\Lambda$, respectively, separate the fluid domain into three regions: the annular area adjacent to the shaft; the kidney-shaped backflow region; and the annular region adjacent to the casing. Table 1 lists the areas of each of these three regions as a fraction of the total area for various values of $\bar{e}$ and $\bar{\Omega}$.

A more complete catalogue of formulae and streamline plots, including ones for the non-counter-rotating cases, may be found in Ballal & Rivlin (1976). The reader may also find the relevant quantities in Kaper (1991, Part II, Appendix A).

## 3. Modulation protocols

Throughout this work, we use the following two representative modulation protocols:

$$\Omega_1(\epsilon t) = 1, \quad \Omega_2(\epsilon t) = -6 + 4\cos(\epsilon t), \tag{MP1}$$

$$\Omega_1(\epsilon t) = 1, \quad \Omega_2(\epsilon t) = -30.5 + 29.5\cos(\epsilon t), \tag{MP2}$$

where $0 < \epsilon \ll 1$. With the choice of (MP1) and (MP2), we operate well within the range of angular velocities for which Ballal & Rivlin (1976) report their results. Also, quasi-steadiness is maintained when the Stokes number $St = \epsilon L^2/\nu$ is small.

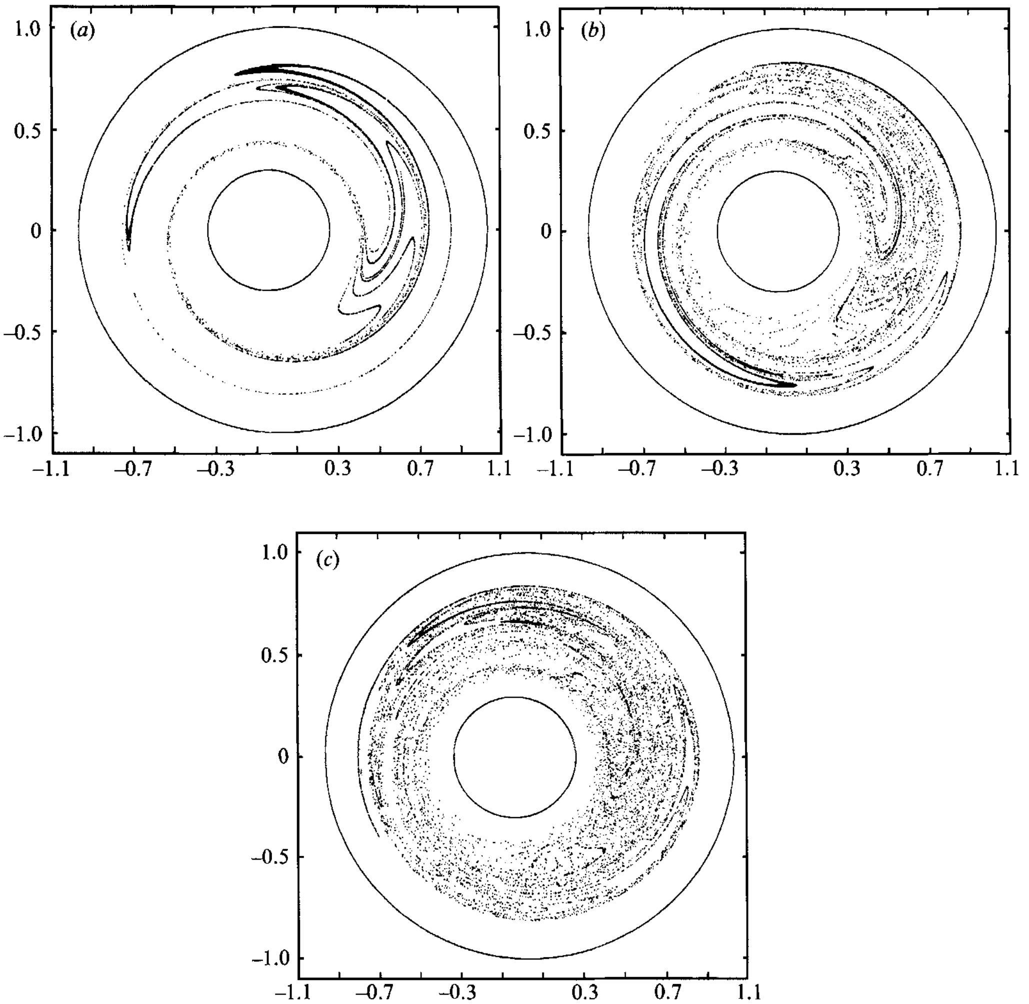

FIGURE 2. A patch of tracer dye, initially located in a circle in the mixing zone, evolves into a highly striated and folded structure. We show the patch at the end of the first, second, and third periods of the modulation, i.e. at times $z = 2\pi$, $4\pi$ and $6\pi$ in (*a*), (*b*) and (*c*) respectively. Flow parameters: $\bar{e} = 0.1$, $\bar{r} = 0.3$, $\epsilon = 2\pi/30$, and we used (MP1).

Introduction of the modulation protocols makes the (2.1) non-integrable (see figure 2 for an example) and puts them in the form of an adiabatic dynamical system:

$$\dot{x} = \frac{\partial\psi}{\partial y}(x,y;\Omega_1(z),\Omega_2(z)), \quad \dot{y} = -\frac{\partial\psi}{\partial x}(x,y;\Omega_1(z),\Omega_2(z)), \quad \dot{z} = \epsilon, \tag{3.1}$$

where the dependence of $\psi$ on $z$ is through the slowly varying time-dependent functions $\Omega_1(z)$ and $\Omega_2(z)$ given by the modulation protocols. Since the modulation protocols are periodic in $z = \epsilon t$ and (3.1) is Hamiltonian, we use the area-preserving Poincaré map

$$T_{z_0}\begin{pmatrix} x(z_0) \\ y(z_0) \end{pmatrix} \equiv \begin{pmatrix} x(z_0+2\pi) \\ y(z_0+2\pi) \end{pmatrix}$$

with $z_0 \in [0, 2\pi)$, which gives a stroboscopic picture of the fluid domain.

The flow parameter introduced by these modulations is $\Delta\bar{\Omega} \equiv \max_{z\in[0,2\pi)} \bar{\Omega}(z) - \min_{z\in[0,2\pi)} \bar{\Omega}(z)$. It measures the amplitude of the modulation, since the ratio of $\Omega_2$

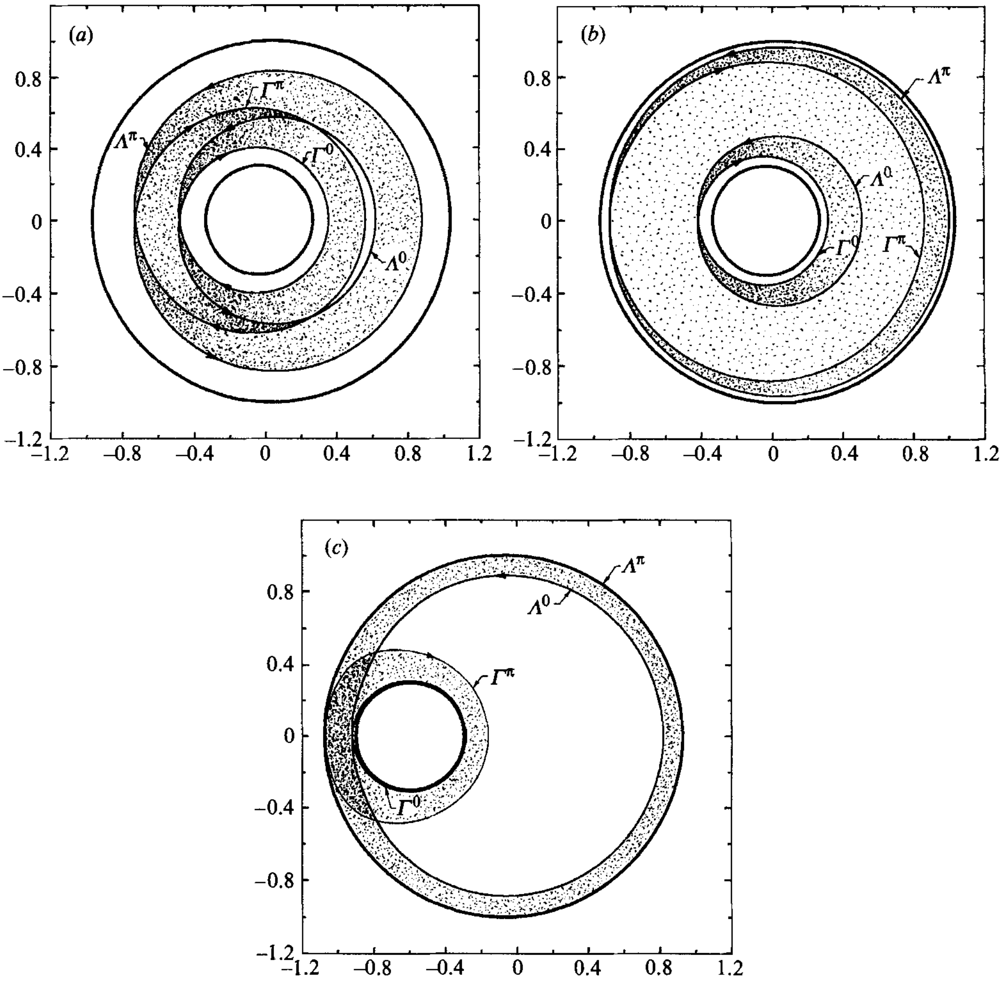

FIGURE 3. Potential mixing zones (shaded regions) for various parameters. (*a*) $\bar{\epsilon} = 0.1$ with (MP1); (*b*) $\bar{\epsilon} = 0.1$ with (MP2); (*c*) $\bar{\epsilon} = 0.75$ with (MP1). Note that in (*c*), $\Gamma^0$ and $\Lambda^{\pi}$ nearly coincide with the inner and outer cylinders, respectively. In all frames, $\bar{r} = 0.3$.

to $\Omega_1$ determines the location of the instantaneous saddle, see figure 3. For (MP1), $\Delta\bar{\Omega} = 8$ because $\bar{\Omega}(z)$ varies in the interval $[-2, -10]$, and $\Delta\bar{\Omega} = 59$ for (MP2) because $\bar{\Omega}(z)$ varies in the interval $[-1, -60]$. Hence, (MP1) is a 'moderate' modulation, because the instantaneous saddle stagnation point moves slowly and periodically across a moderately large fraction of the gap between the cylinders, and (MP2) is a 'strong' modulation, because the instantaneous saddle stagnation point moves slowly and periodically across almost the entire gap between the cylinders.

(MP1) and (MP2) have been chosen so that their implementation is the simplest experimentally. A computer-controlled stepping motor may be used to change the angular velocities of the inner cylinder many times per modulation period (L. G. Leal 1989, personal communication). The apparatus described in Swanson & Ottino (1990) has this capacity.

Experimental run times for (MP1) and (MP2) may be determined as follows. With $\epsilon = 0.14$, and with the choice of moderate modulation (MP1), for example, the modulation period is $2\pi/\epsilon \approx 44.9$ non-dimensional time units, which is the longest modulation period for which good mixing is observed since $\epsilon = 0.14$ is the smallest $\epsilon$ in the good parameter range. In this time, the outer and inner cylinders make approximately 45 and 269 revolutions, respectively. To convert to real time, assume $R_1 = 7.5$ cm and $\bar{r} = 0.3$, and let the fluid be Chlorowax 45, a chlorinated paraffin from Diamond Shamrock often used as a solvent for polymers, which has $\rho = 1.3$ g/cm$^3$ and $\mu = 190.0$ P. Then, $Re = 1$ is obtained with an angular velocity of 0.7 revolutions per s, and one modulation period is approximately 386 s.

A concept used often in the remainder of the present work is that of an *instantaneous streamline*. The instantaneous streamline is the closed trajectory the particle would execute if the system evolved with the value of $z$ frozen at its instantaneous value. Thus, it coincides with the orbit of the steady-state flow (with $\Omega_1$ and $\Omega_2$ equal to their value at the instantaneous value of $z$) that passes through the particle's instantaneous position. Of course, since particle paths in the modulated flow no longer coincide with streamlines, this concept is a fictitious one; nevertheless it is often used in adiabatic dynamical systems, see Kaper & Wiggins (1991*a*) and Escande & Elskens (1991), and it is helpful in the context of quasi-steady Stokes flows, as well. The inner and outer instantaneous stagnation streamlines at the instant of slow time $z$ are denoted $\Gamma^z$ and $\Lambda^z$, respectively. The analogous concept exists for *instantaneous stagnation points*.

## 4. Location and size of the mixing zone

Although the four flow parameters $\bar{e}$, $\Delta\bar{\Omega}$, $\bar{r}$, and $\epsilon$ are mutually independent, the search for the combination of them which yields a predetermined mixing zone requires that we study their effects simultaneously. In §4.1, we begin by considering the influence of the first three parameters and define the concept of a *potential mixing zone*. Then, in §§4.2–4.4, we add to these considerations the influence of $\epsilon$, which determines how much of the area potentially available for mixing is actually used.

As an example to illustrate the control over the mixing process, we focus at various points in this section on the problem of maximizing the mixing zone size. In the counter-rotating regime, for the geometry with $\bar{r} = 0.3$, the largest possible mixing zone is obtained when the parameters are chosen such that: $\bar{e} \approx 0.1$; $\Delta\bar{\Omega}$ is large, so that $\bar{\Omega}(z)$ varies in an interval which is finite, negative, and as large as possible, on the order of $[-1, -60]$ as in (MP2); and $\epsilon$ is moderately small, but not too small, for this example, in the interval $0.14 \leqslant \epsilon \leqslant 0.34$, see figure 3(*b*). With this choice of parameters the mixing zone occupies virtually the entire fluid domain. Also, islands in this zone are negligibly small for this optimal choice of parameters.

### 4.1. *The parameters $\bar{e}$ and $\Delta\bar{\Omega}$ and the potential mixing zone*

In much of the $O(1)$ area swept out by the (fictitious) instantaneous streamlines, the theory of adiabatic invariance and Arnol'd's extension of the KAM theorem to adiabatic Hamiltonian systems are not applicable because one of the main assumptions that those theories rely on ceases to be valid on and near stagnation streamlines, which are zero-frequency orbits. The violated assumption is that the frequency of the instantaneous steady-state orbits be one order of magnitude larger, i.e. $O(1)$, than the modulation frequency $\epsilon$. Observations collected from theoretical and numerical work on various model problems in physics (see Cary, Escande & Tennyson 1986; Cary & Skodje 1989; Bruhwiler & Cary 1989; Kaper & Wiggins 1991*a*, and Elskens & Escande 1991) suggest that tracer particles can explore most of this swept-out area because there are very few barriers to their transport in this region. Hence this is the region in which mixing can be expected to occur. We caution, however, that there is a piece of the

| $\bar{\epsilon}$ | Protocol | Total area (%) |
|---|---|---|
| 0.1 | MP1 | 57.5 |
| 0.1 | MP2 | 87.3 |
| 0.3 | MP1 | 53.0 |
| 0.5 | MP1 | 40.2 |
| 0.5 | MP2 | 75.9 |
| 0.75 | MP1 | 18.9 |
| 0.75 | MP2 | 33.5 |

TABLE 2. Area of the potential mixing zone as a function of $\bar{\epsilon}$ and the modulation protocol. The area of the entire domain is 2.8588 scale units and the potential mixing-zone area is given as a percentage of the total fluid domain.

swept-out area in which adiabatic invariance does apply despite the fact that there are instantaneous separatrices there. In §4.2, we make this precise.

For (MP1) and (MP2), the region swept out may be specified exactly as

$$(\textstyle\bigcup_{z\in[0,\pi]}\Gamma^z)\bigcup(\textstyle\bigcup_{z\in[0,\pi]}\Lambda^z), \tag{4.1}$$

where $\Gamma^z$ and $\Lambda^z$ denoted the inner and outer instantaneous stagnation streamlines at time $z$. Because the measure of the set (4.1) is to leading order the area potentially available for mixing, the set (4.1) is called the *potential mixing zone*, see figure 3 and table 2.

The symmetry in (MP1) and (MP2) about $z = \pi$, namely $\bar{\Omega}(z) = \bar{\Omega}(2\pi - z)$ for $z \in (\pi, 2\pi]$, implies that we only need to take the unions over $z \in [0, \pi]$ in (4.1). For more general protocols, the unions are taken over all $z$ between the two values of $z$ corresponding to an instantaneous separatrix which locally (i.e., compared to the instantaneous separatrices for nearby values of $z$) encloses a maximum area and an instantaneous separatrix which locally encloses a minimum area (see Kaper & Wiggins 1991*a*).

Pursuing the example of maximizing the size of the mixing zone, we see from the data in table 2 that the choice of $\bar{\epsilon} \leqslant 0.1$, combined with prescribing $\bar{\Omega}(z)$ to vary in the largest possible finite negative interval, maximizes the size of the potential mixing zone.

### 4.2. *The parameter* $\epsilon$ *and the actual mixing zone*

We focus throughout the following subsections on the sample case $\bar{\epsilon} = 0.1$, $z_0 = 0 \bmod 2\pi$, and in which (MP1) is used. This choice is made for illustrative purposes only. There exist two qualitatively different regimes – one, corresponding to small values of $\epsilon$ ($\epsilon < 0.1$ in this sample case) in which the actual mixing zone is considerably smaller than the potential mixing zone, see figure 4(*b*), and the other corresponding to moderate values of $\epsilon$ ($0.14 \leqslant \epsilon \leqslant 0.34$ for this sample case) in which the actual mixing zone is as big as the potential mixing zone, see figure 4(*a*). The value of the lower bound of the moderate range ($\epsilon = 0.14$ for the sample case) can be obtained analytically by knowing the thickness of the minimal backflow region; i.e. before experiments or numerical simulations are performed. The transition between the small and medium size $\epsilon$ regimes ($0.1 < \epsilon < 0.14$ for the sample case) is smooth.

For $\epsilon$ small, a large part of the minimal instantaneous backflow region appears to be a regular zone, and the actual mixing zone is smaller than the potential zone (4.1). Thus, we show that for small $\epsilon$, the actual mixing zone is equal to the potential mixing zone minus most of the minimal backflow region except the strip $S_1^\epsilon$ plus the strips $S_2^\epsilon$ and $S_3^\epsilon$ around the inner and outer peripheries of the potential mixing zone.

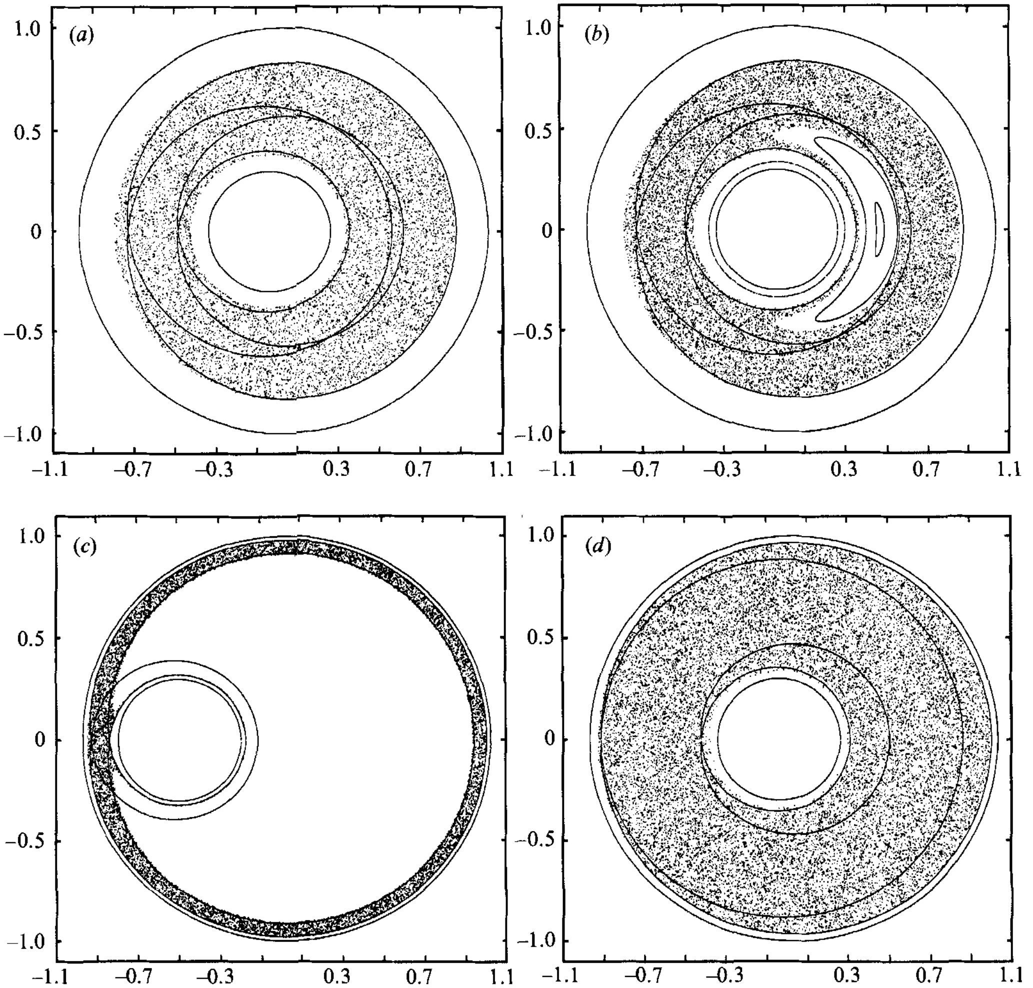

FIGURE 4. Actual mixing zones (all with $\bar{r} = 0.3$, and all have the instantaneous stagnation streamlines $\Gamma^0, \Lambda^0, \Gamma^\pi$, and $\Lambda^\pi$ superimposed): (*a*) $\bar{e} = 0.1$, $\epsilon = 2\pi/40$, with (MP1); integrated one point for 10000 periods. (*b*) $\bar{e} = 0.1$, $\epsilon = 2\pi/120$, with (MP1); integrated one point for 10000 periods. The instantaneous backflow region contains a large regular zone. (*c*) $\bar{e} = 0.75$, $\epsilon = 2\pi/60$, with (MP1); integrated one point for 10000 periods. (*d*) $\bar{e} = 0.1$, $\epsilon = 2\pi/40$, with (MP2); integrated one point for 20000.

Consider that part of the backflow region in which the orbital frequency $\omega$ is much larger than the modulation frequency $\epsilon$. Adiabatic invariance theory states that a tracer particle will move slowly from one instantaneous streamline to the next, but always in such a way that the area enclosed by these streamlines is the same to leading order (to $O(\epsilon/\omega)$). If the tracer particle is injected at the initial value of the slow time $z_1$, we denote the area enclosed by the instantaneous periodic streamline that it starts on by $A_{po}(z_1)$. Now, because the instantaneous backflow region increases and decreases in size periodically during the modulation, only those orbits for which $A_{po}(z_1)$ is sufficiently less than the area occupied by minimum backflow region, where the minimum is taken over all $z$, stay in this region for all times and have an adiabatic invariant. See table 1 for an example with $\bar{e} = 0.1$ and (MP1) for which the backflow region occupies minimal area at $z = 0 \bmod 2\pi$ and the area occupied is 16.5%.

| $\epsilon$ | $\epsilon^2 \ln^2(1/\epsilon)$ | $\Lambda^z$ layer | $\Gamma^z$ layer |
|---|---|---|---|
| 0.105 | 0.056 | 0.050 | 0.126 |
| 0.052 | 0.024 | 0.016 | 0.037 |
| 0.035 | 0.014 | 0.005 | 0.027 |

TABLE 3. Thickness of the layer $S_1^\epsilon$ for $\bar{e} = 0.1$ and $\bar{r} = 0.3$, with (MP1).

Arnol'd's extension of the KAM theorem (see Arnol'd, Neishtadt & Kozlov 1988 for an exposition) for slow, periodic and quasi-periodic modulations gives slightly more information. This theory applies to quasi-steady Stokes flows since all of the orbits in the steady-state back-flow region satisfy a twist condition, $(\mathrm{d}\omega/\mathrm{d}I)(I, z) \neq 0$ for all $z$, where $\omega$ is the frequency of the unperturbed orbit with action $I$. In particular, the theory states that most of the orbits for which $A_{po}(z_1)$ is sufficiently less than the size of the minimal backflow region lie on invariant tori. Arnol'd introduced a sequence of transformations, including an averaging-based coordinate change, to bring the equations of motion of an adiabatic system into the standard form for KAM theory, although they constitute properly degenerate systems. Using this transformation, he proved that most of the unperturbed periodic orbits survive as invariant tori (Arnol'd tori) on which orbits evolve quasi-periodically. For adiabatic systems, 'most' implies that the part of phase space in which there are no tori on the Poincaré section has a total size of $O(e^{-c/\epsilon})$ as $\epsilon \rightarrow 0$ where $c$ is a constant which satisfies $c > 0$. In particular, the ribbons of stochasticity in between adjacent tori must be transcendentally narrow annuli. We label an area which is covered by these persistent tori as a *regular zone*.

Thus, excluding an annular strip around the inside of the periphery of the instantaneous backflow region, the Arnol'd tori occupy all but some exponentially vanishing part. We must exclude the region occupied by tori from the actual mixing zone. We show a case in which the minimum backflow region contains a large regular zone in figure 4(*c*).

This is the first explanation of the highly integrable appearance of regular zones in quasi-steady Stokes flows. In fact, in the singularly perturbed case, a regular zone looks much more integrable than a regular zone in the regularly perturbed case. This difference in appearance arises because in regularly perturbed systems (i.e. those derived from a Hamiltonian $H = H_0(p, q) + \delta H_1(p, q, t)$, with scalar $p$ and $q$ and $0 < \delta \ll 1$) the regions in between any pair of invariant tori are generically $O(\delta^{\frac{1}{2}})$ in width.

### 4.3. *The layer $S_1^\epsilon$ and the transition regime to moderate $\bar{\epsilon}$*

In this subsection, we discuss the orbits which lie in a layer, $S_1^\epsilon$, just inside the boundary of the minimal backflow region, see figure 4(*b*) for example. The thickness of $S_1^\epsilon$, which cannot be obtained from the theories cited above, is exactly what we need in order to completely determine the size of the mixing zone for small $\epsilon$.

$S_1^\epsilon$ has an annular shape. Its inner boundary is the outermost (or last) Arnol'd torus in the minimal backflow region, and on the outside it is adjacent to the potential mixing zone. Thus, as may be seen in the figures, it forms part of the actual mixing zone. We report the values for the thickness of $S_1^\epsilon$, as measured along the $x$-axis in the wide part of the gap between the shaft and the casing, obtained from our numerical simulations for various of the canonical cases in table 3. The data indicate that the width of $S_1^\epsilon$ vanishes at least as fast as $\epsilon$ when $\epsilon \rightarrow 0$.

While a general theory is not yet available to give the asymptotic scaling of $S_1^\epsilon$ for $\epsilon \rightarrow 0$, Neishtadt, Chaikovshii & Chernikov (1991), have extended their work and that of Cary *et al.* (1986), and shown for a model problem that the layer which corresponds to $S_1^\epsilon$ in this problem is $O(\epsilon^2|\ln 1/\epsilon|^2)$ as $\epsilon \to 0$. One can try to fit the data from one case ($\bar{e} = 0.1$, $\bar{r} = 0.3$, (MP1) with various values of $\epsilon$ for $\epsilon < 0.14$) – see table 3 – to this functional dependence on $\epsilon$; however, the fit is not good. This completes the discussion of the location and size of the mixing zone for small $\epsilon$.

Because the minimal backflow region has a kidney-like shape and the layer $S_1^\epsilon$ is inside its boundary, there exists some critical value of $\epsilon$ at which $S_1^\epsilon$ is as thick as the half-width of the backflow region. The plots and data show that the regularly appearing backflow region becomes smaller as $\epsilon$ grows from being very small (less than 0.1), looks like a tiny island for $\epsilon \approx 0.13$ (see Kaper 1991, Part II, figure 2.4), and ceases to exist altogether for $\epsilon \geqslant 0.14$. Thus, this critical value is approximately $\epsilon = 0.14$ in the sample case.

When $\epsilon$ attains moderate values, the actual mixing zone is at least as big as the potential mixing zone. For $0.14 \leqslant \epsilon \leqslant 0.34$, our numerical simulations show that the entire backflow region belongs to the mixing zone, see figure 4(*a*). Therefore, for moderate $\epsilon$, the actual mixing zone is the potential mixing zone plus the layer $S_1^\epsilon$ around the outer periphery of the potential mixing zone.

### 4.4. *The optimal parameter choice*

When $\epsilon$ attains moderate values, we have already seen in figure 4(*a*) that the actual mixing zone is at least as big as the potential mixing zone, because the entire backflow region belongs to the mixing zone. The conclusions made in the above discussion of the layer $S_1^\epsilon$ apply with suitable modifications to the layers, $S_2^\epsilon$ and $S_3^\epsilon$, around the inner and outer boundaries, respectively, of the potential mixing zone also, boundaries which are formed by the instantaneous stagnation streamlines $\Gamma^0$ and $\Lambda^\pi$. The other boundaries of the layers $S_2^\epsilon$ and $S_3^\epsilon$ are the extremal Arnol'd tori of the families of tori adjacent to the casing and the shaft, respectively. Thus, for moderate $\epsilon$, the actual mixing zone is larger than the set (4.1).

The theory and data therefore establish the claims we made about the sample case at the beginning of §4. By choosing a small value of the eccentricity, $\bar{e} \leqslant 0.1$, by prescribing that $\bar{\Omega}(z)$ vary over a large negative interval such as the one in (MP2), and by using a moderate, but not too small, modulation frequency, we can obtain a mixing zone which is as large as possible for the counter-rotating eccentric journal bearing. From our steady-state measurements we saw how to optimize the potential mixing zone so that it occupies virtually the entire fluid domain, and from adding the considerations involving the parameter $\epsilon$, we have shown that the actual mixing zone is slightly bigger than the potential one with this optimal choice of parameters.

When (MP2) is used, a similar dependence on $\epsilon$ is found, although the lower bound on the range of 'moderate' $\epsilon$ is smaller for (MP2) than it is for (MP1) in the same geometry, see Kaper (1991, of Part II, figure 2.13). This is because the smallest value of $\epsilon$ for which $S_1^\epsilon$ is wider than the minimal backflow region using (MP2) is less than that when using (MP1). The lower bound for (MP2) with the given values of $\bar{e}$ and $\bar{r}$ is less than 0.14. Also, the results for different $\bar{e}$ will be qualitatively similar to those we obtained for the sample case $\bar{e} = 0.1$ and can be obtained with the methods used here.

### 4.5. *The fluid domains adjacent to the cylinders*

The fluid in the annular regions adjacent to the two cylinders evolves in an integrable way. Arnol'd's extension of KAM theory cited in §4.2 applies to the orbits in these regions and states that they lie on tori which are exponentially close to each other. The boundaries of these regular regions adjacent to the cylinders are the outermost tori of the family of tori which make up these zones, see figure 7(*b*). Thus, together with the mixing zone and the backflow region, these two regular zones account for the entire fluid domain.

## 5. Transport analysis

The homoclinic tangles and lobes in slowly modulated (singularly perturbed) systems are both qualitatively and quantitatively very different from those studied in weakly perturbed systems, i.e. systems to which the usual Melnikov theory applies and about which much has been written (see Wiggins 1992 and the literature cited there for examples). Chief among the differences is that the lobes are very long and thin – in particular what we will define as the turnstile lobes are of length $O(1/\epsilon)$ and area $O(1)$ so that their average width is $O(\epsilon)$ asymptotically as $\epsilon \rightarrow 0$, as we show in §§6.2 and 6.3, and each successive image (both forward and backward) of a turnstile lobe is longer and thinner than the preceding image, while having the same area due to the area-preservation property of the Poincaré map. This stands in contrast with the usual (regular-perturbation) systems in which the lobe area is $O(\delta)$, where $\delta$ is the amplitude of the small perturbation. As we see in our numerical simulations and in the experiments and numerical simulations with blinking protocols, tracer fluid appears to follow the unstable manifolds, see figure 5, deforming itself into a kind of fattened unstable manifold, i.e. a strip of tracer is thicker than the corresponding segment of the unstable manifold (at least for finite times). In the following sections, we show that for continuous modulation protocols these fattened regions are lobes. Thus, we refine the notions in the quasi-steady Stokes literature that transport occurs along unstable manifolds.

In addition, the singular-perturbation nature of these modulated flows implies that lobe area is the inter-regional flux per half period, and as a result, the transport in these flows is more complicated than in the usual case in which transport is studied every full period only. The half-period analysis we present here was first announced in Kaper & Wiggins (1989) and represents the first fluid mechanical application of the methods developed in Elskens & Escande (1991) and Kaper & Wiggins (1991*a*).

The last difference we mention is that the turnstiles permeate the entire mixing zone, causing the tangle to function as its 'backbone', because the tangle sweeps out the entire $O(1)$ separatrix-swept area. This is also in marked contrast with the usual, regular-perturbation case where the turnstile lobes only cover some $O(\delta)$ fraction of the stochastic layer. This unique feature of adiabatic dynamical systems guarantees that large-scale mixing occurs within the first few periods of the modulation.

### 5.1. *Structures in adiabatic dynamical systems*

The saddle stagnation point of the steady flow with $z = z_0$ persists as the saddle stagnation point $X_\epsilon(z_0)$ of the Poincaré map $T_{z_0}$, i.e. as a periodic trajectory of the flow, see figure 6 in which $z_0 = 0$. Wiggins (1988*a*, *b*) contain expositions of the theory specific to adiabatic dynamical systems. Since $X_\epsilon(z_0)$ lies near $X_0(z_0)$, one can construct an asymptotic expansion in powers of $\epsilon$ for its position as a function of $z$, see Kaper (1991, Part II, Appendix B). The leading-order term is $X_0(z_0)$, and the first correction term is $O(\epsilon)$ in the $y$-component and $O(\epsilon^2)$ in the $x$-component. Furthermore, from symmetry considerations, $X_\epsilon(z_0)$ lies on the $x$-axis for $z_0 = 0 \bmod 2\pi$ and for $z_0 = \pi \bmod 2\pi$.

If one were to watch the experiment continuously as $z$ increases from $z_0$ to $z_0 + 2\pi$, instead of sampling it stroboscopically with the Poincaré map, one would see that the

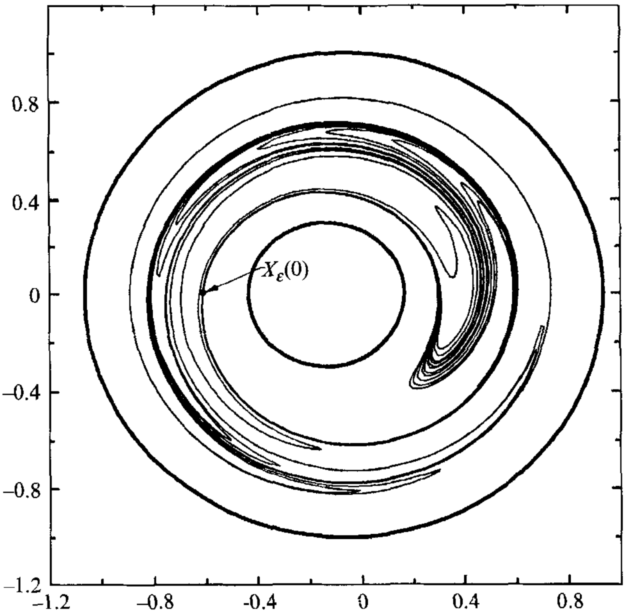

FIGURE 5. Piece of the unstable manifold $\Gamma^U(X_\epsilon(0))$ for the flow with $\epsilon = 2\pi/40$, (MP1), $\bar{e} = 0.1$, and $\bar{r} = 0.3$.

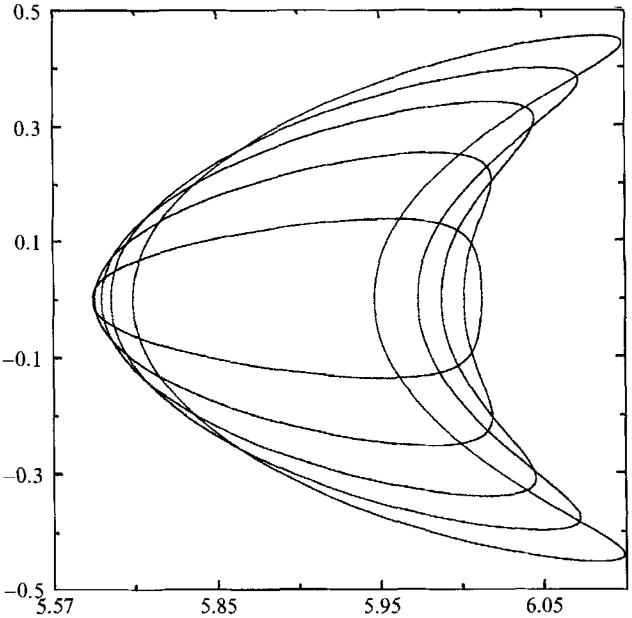

FIGURE 6. The orbit $\gamma_\epsilon(z)$ for various $\epsilon$ with $\bar{e} = 0.1$, $\bar{r} = 0.3$ and (MP1). The instantaneous stagnation point executes clockwise motion along the indicated curves. The curve with the largest maximum vertical coordinate is for $\epsilon = 2\pi/20$, and in descending order, the others are for $\epsilon = 2\pi/30$, $2\pi/40$, $2\pi/60$, $2\pi/120$, respectively.

saddle executes a periodic orbit $\gamma_\epsilon(z)$. Figure 6 illustrates the orbit $\gamma_\epsilon(z)$ for various values of $\epsilon$. This closed path lies in the fluid domain inside a strip of width $O(\epsilon)$ around the segment $[X_0(z_0 = \pi), X_0(z_0 = 0)]$ on the $x$-axis in the narrow gap between the shaft and the casing in the mixing zone.

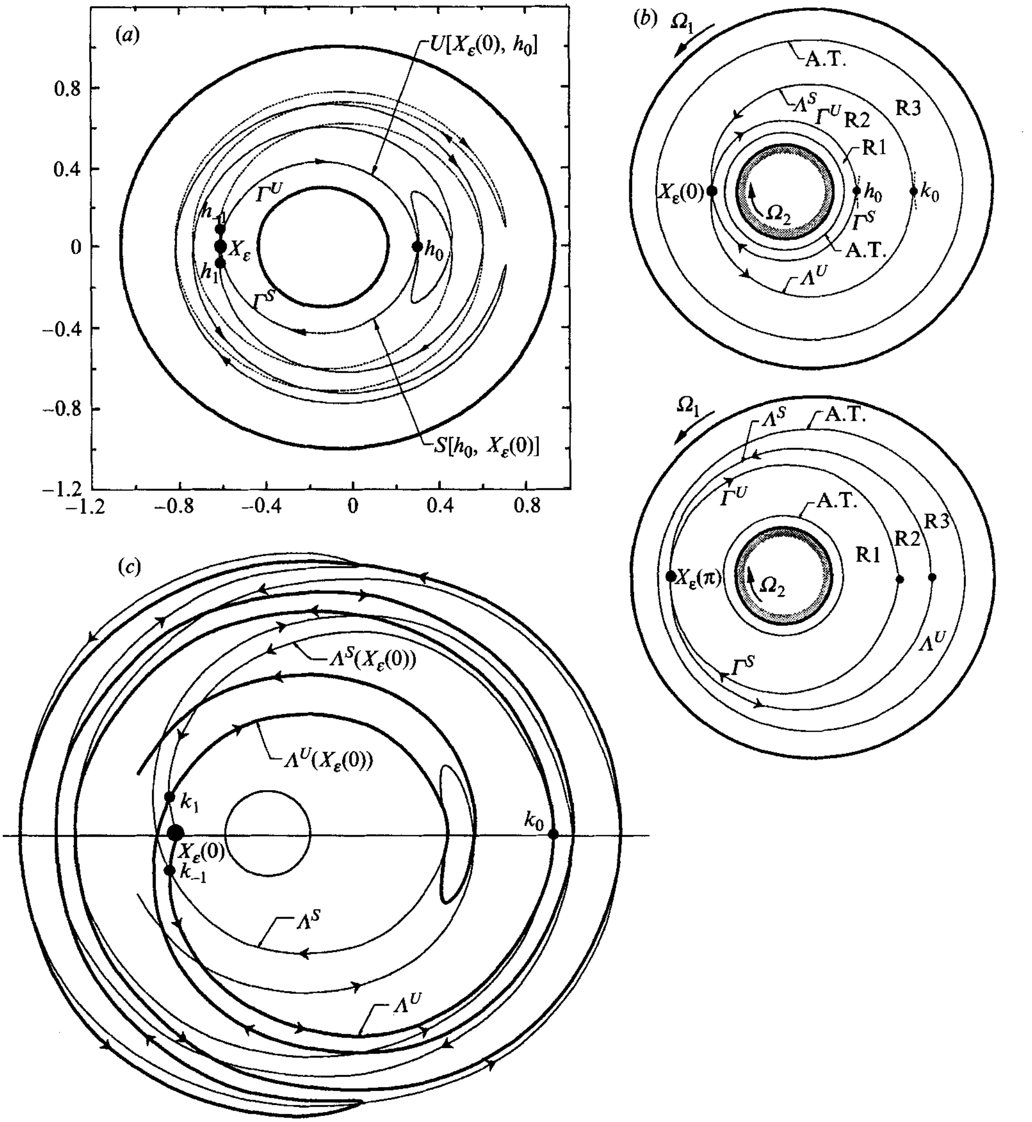

FIGURE 7. $\bar{\epsilon} = 0.1$, $\bar{r} = 0.3$, $\epsilon = 2\pi/40$, and (MP1). (*a*) Segments of the stable and unstable manifold, the pips $h_i$ for $i = -1, 0, 1$. $h_1$ and $h_{-1}$ are exponentially close (in $\epsilon$) to $X_\epsilon$. (*b*) The regions R1–R3, for $z = 0$ in the top picture and for $z = \pi$ in the bottom frame. AT denotes the extremal Arnol'd torus. The annular regions between the cylinders and these extremal tori (i.e. complementary to R1–R3) are regular zones filled with tori exponentially close to each other. (*c*) A schematic of the homoclinic tangle formed by $\Lambda^U$ and $\Lambda^S$.

Introduction of the time modulation breaks the coincidental stable and unstable manifolds (stagnation streamlines) $\Lambda^{z_0}$ and $\Gamma^{z_0}$ and causes them to intersect transversely. There exist four infinitely long distinguished manifolds which intersect in two intertwined homolinic tangles, see figure 7. These manifolds may be seen experimentally as the streaklines one obtains by injecting tracer dye at a point on the instantaneous unstable eigenspace extremely close to the slowly moving saddle point. Two of the manifolds consist of all of the points in the fluid domain which are forward ($n \rightarrow +\infty$, where $n$ is the discrete time of the Poincaré map) asymptotic to $X_\epsilon(z_0)$. We label these

$\Gamma^S(X_\epsilon(z_0))$ and $A^S(X_\epsilon(z_0))$ because they are the stable manifolds of $X_\epsilon(z_0)$ and remnants of the branches of the stable manifolds of $X_0(z_0)$ which coincide with $\Gamma^{z_0}$ and $A^{z_0}$, respectively. The other two, $\Gamma^U(X_\epsilon(z_0))$ and $A^U(X_\epsilon(z_0))$, consist of points that are backward ($n \rightarrow -\infty$) asymptotic in time to $X_\epsilon(z_0)$. They are the unstable manifolds of $X_\epsilon(z_0)$. Although one only observes the unstable manifolds in experiments, one can obtain the stable manifolds from symmetry considerations for special $z_0$ ($z_0 = 0$, $\pi \bmod 2\pi$ for (MP1) and (MP2)) and in general by performing a second experiment in which the direction of rotation of the two cylinders is reversed.

The point $h_0$, where $\Gamma^U(X_\epsilon(z_0))$ and $\Gamma^S(X_\epsilon(z_0))$ intersect, and the point $k_0$, where $A^U(X_\epsilon(z_0))$ and $A^S(X_\epsilon(z_0))$ intersect, may be chosen arbitrarily, see figure 7. For convenience, we choose them to be the intersection points lying on the $x$-axis. We label the segment of $\Gamma^U(X_\epsilon(z_0))$ between $X_\epsilon(z_0)$ and $h_0$ by $U[X_\epsilon(z_0), h_0]$ and that of $\Gamma^S(X_\epsilon(z_0))$ between $X_\epsilon(z_0)$ and $h_0$ by $S[X_\epsilon(z_0), h_0]$. Similarly, $U[X_\epsilon(z_0), k_0]$ denotes the segment of $\Gamma^U(X_\epsilon(z_0))$ between $X_\epsilon(z_0)$ and $k_0$, and $S[X_\epsilon(z_0), k_0]$ denotes that of $\Gamma^S(X_\epsilon(z_0))$ between $X_\epsilon(z_0)$ and $k_0$. Here, $h_0$ and $k_0$ are *primary* homoclinic points $p$ in the sense that $U[X_\epsilon(z_0), p]$ and $S[X_\epsilon(z_0), p]$ intersect only in the point $p$. For a review of intersections in heteroclinic tangles see Rom-Kedar & Wiggins (1990).

With the choice of $z_0 = 0 \bmod 2\pi$, the symmetry of the Poincaré map

$$n \rightarrow -n, \quad x \rightarrow x, \quad y \rightarrow -y$$

is such that the unions

$$\left.\begin{aligned} B_{1,2} &\equiv U[X_\epsilon(z_0), h_0] \cup S[X_\epsilon(z_0), h_0], \\ B_{2,3} &\equiv U[X_\epsilon(z_0), k_0] \cup S[X_\epsilon(z_0), k_0] \end{aligned}\right\} \tag{5.1}$$

naturally divide the mixing zone into three regions in the time-periodic flow, see figure 7(*b*). Region 1 (R1) is the annular domain bounded on the inside by the outermost Arnol'd torus of the family of tori which make up the regular zone adjacent to the shaft and on the outside by $B_{1,2}$. The kidney-shaped domain in the middle of the mixing zone bounded on the outside by $B_{1,2}$ and $B_{2,3}$ is region 2 (R2). To completely define it, however, we recall from the previous section that there are two possibilities. Either $\epsilon$ is large enough such that the entire domain between $B_{1,2}$ and $B_{2,3}$ is part of the actual mixing zone, e.g. $\epsilon \geqslant 0.14$ in the case when $\bar{e} = 0.1$, $\bar{r} = 0.3$, and one uses (MP2), or $\epsilon$ is small and there exists a regular region occupying part of the minimal backflow region. In the former case, the entire kidney-shaped domain is R2, and in the latter case, R2 is an annular domain and the inner boundary is the outermost Arnol'd torus in the family of tori which make up the regular zone.

Finally, region 3 (R3) is also an annular domain bounded on the inside by $B_{2,3}$ and on the outside by the smallest Arnol'd torus in the family of tori in the regular zone adjacent to the casing. Thus, the boundaries $B_{1,2}$ and $B_{2,3}$ act as the dividing curve between the three regions. Of course, one can identify three regions and their natural boundaries for every value of $z_0$ in $[0, 2\pi)$, but for simplicity, we focus only on two choices of $z_0$: $z_0 = 0, \pi$.

In contrast to the situation in the steady state, transport between the three regions is possible in the modulated flow. Before showing how the structures we have just identified form a template from which we can determine stretching and transport quantities, we introduce one final concept, that of a turnstile lobe, see figure 8.

Invariance of the manifolds implies that homoclinic points are mapped to homoclinic points under $T_{z_0}$ and its inverse $T_{z_0}^{-1}$. In particular, primary homoclinic points (pips) are mapped to pips, see Rom-Kedar & Wiggins (1990), and thus the streaklines $\Gamma^S(X_\epsilon(z_0))$ and $\Gamma^U(X_\epsilon(z_0))$ intersect each other infinitely many times as $X_\epsilon(z_0)$ is approached from both sides along the stable manifolds, forming a homoclinic tangle, as do the

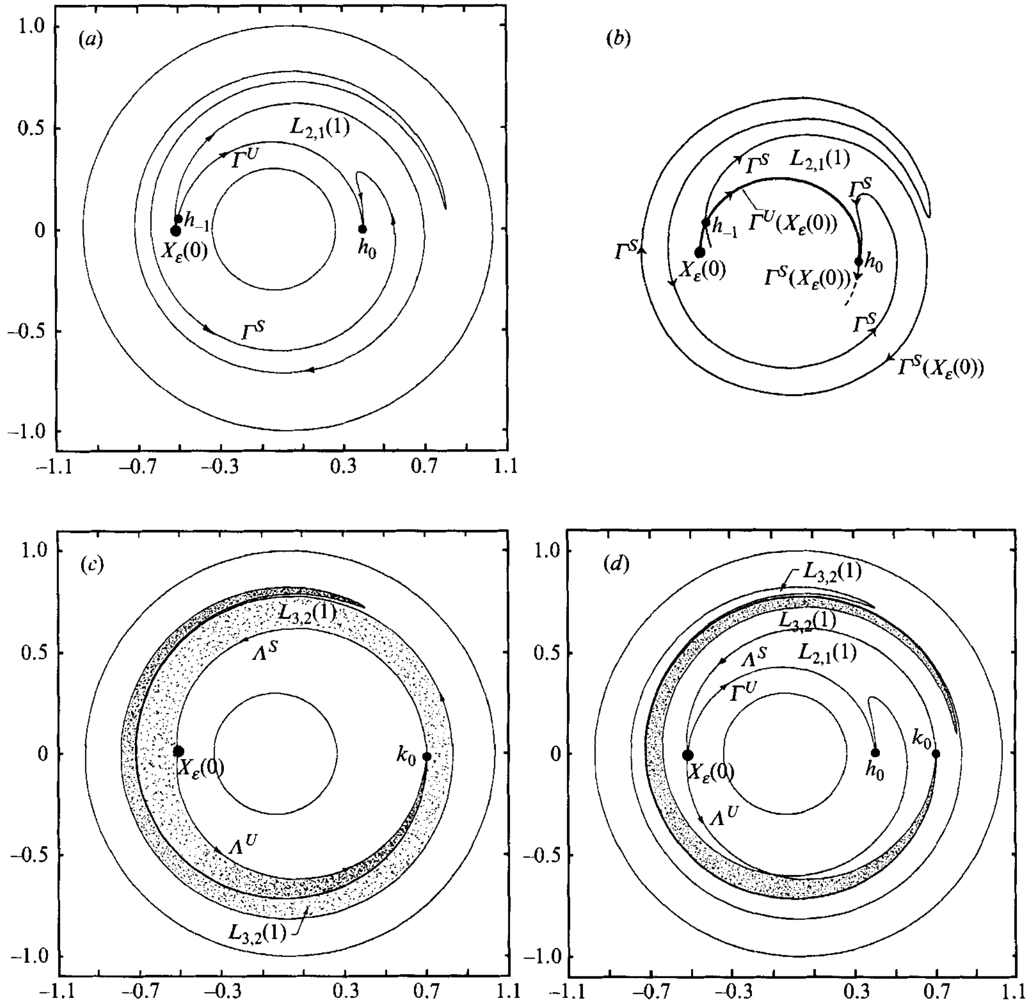

FIGURE 8. The turnstile lobes when $\bar{e} = 0.1$, $\bar{r} = 0.3$, $\epsilon = 2\pi/40$, and (MP1) is used. (*a*) The turnstile lobe $L_{2,1}(1)$ of the $\Gamma$-tangle. The 'tip' of the lobe is in the upper right quadrant of the domain, and the 'base' point is the midpoint of the segment of $\Gamma^U(X_\epsilon)$ between $h_{-1}$ and $h_0$. (*b*) A schematic of (*a*). (*c*) The turnstile lobe $L_{3,2}(1)$ of the $\Lambda$-tangle. (*d*) The intersection of $L_{3,2}(1)$ and $L_{2,1}(1)$ is shaded.

streaklines $\Lambda^S(X_\epsilon(z_0))$ and $\Lambda^U(X_\epsilon(z_0))$. The segments of $\Gamma^S(X_\epsilon(z_0))$ and $\Gamma^U(X_\epsilon(z_0))$, which we label $S[h_i, h_{i+1}]$ and $U[h_i, h_{i+1}]$, between any two adjacent pips $h_i$ and $h_{i+1}$, where $i$ is an integer, bound an area on the Poincaré section which is called a lobe. Similarly, the segments $S[k_i, k_{i+1}]$ and $U[k_i, k_{i+1}]$ of $\Lambda^S(X_\epsilon(z_0))$ and $\Lambda^U(X_\epsilon(z_0))$ form a lobe. Now, because the system is Hamiltonian, and because lobe boundaries are invariant under the Poincaré map, $T_{z_0}$ is an area-preserving diffeomorphism of the fluid domain to itself. Thus, one can show that all of the lobes of a given tangle, i.e. of the $\Gamma$-tangle or of the $\Lambda$-tangle, have the same area.

The lobes which are defined by the segments between $h_{-1}$ and $h_0$ and those between $h_{-2}$ and $h_{-1}$, as well as the corresponding ones between $k_{-1}$ and $k_0$ and between $k_{-2}$ and $k_{-1}$ of the $\Lambda$-tangle, play a special role in the stretching and transport of fluid. We refer to them as turnstile lobes.

### 5.2. *Transport in half-period intervals*

The geometrical mechanisms convecting particles from one region to another are the turnstile lobes. As we stated in the previous subsection both the $\Gamma$- and the $\Lambda$-tangles have a pair of turnstile lobes. In this and the next section, we prove that the pair of lobes $L_{1,2}(1)$, defined by $h_{-2}$ and $h_{-1}$, and $L_{2,1}(1)$, defined by $h_{-1}$ and $h_0$, respectively govern the transport out of and into R1, and the pair of lobes $L_{2,3}(1)$ and $L_{3,2}(1)$, defined by the pairs $k_{-2}$ with $k_{-1}$ and $k_{-1}$ with $k_0$, respectively govern the transport into and out of R3. The subscripts on the lobe $L$ refer to the regions.

During the first half of the modulation period, the areas of R1 and R2 increase, while that of R3 decreases. For example, as we see from figure 3 and table 1, the area enclosed by the instantaneous $\Gamma^z$ increases as $\Gamma^z$ sweeps outward away from the shaft for $z$ increasing from 0 to $\pi$. Only those tracer particles which are in lobe $L_{2,1}(1)$ (which is a subset of R2 and R3) at time $z = 0 \bmod 2\pi$ and enter into R1 in one half-period. Similarly, only those particles which are in lobe $L_{3,2}(1)$ (which is a subset of R3) at time $z = 0 \bmod 2\pi$ will be in R2 and R1 at time $z = \pi \bmod 2\pi$.

An analogous result is true for the remainder of the modulation period. During the second half of the period, the above is reversed, because the areas of R1 and R2 decrease, while that of R3 increases. The area enclosed by the instantaneous $\Gamma^z$ decreases.

The mechanisms by which fluid exits these regions are turnstile lobes. In particular, only those tracer particles which are in lobe $L_{1,2}(1)$ (which is a subset of R1) at time $z = \pi \bmod 2\pi$ enter into R2 and R3 during the second half of the modulation period and lie entirely in those regions at time $z = 0 \bmod 2\pi$. Similarly, only those particles which are in lobe $L_{2,3}(1)$ (which is a subset of R2 and R1) at time $z = \pi \bmod 2\pi$ will lie completely in R3 at time $z = 0 \bmod 2\pi$.

To illustrate the above statements, we examine the case in which $\bar{e} = 0.1$, $\bar{r} = 0.3$, $\epsilon = 2\pi/40$, and (MP1) is used, see figure 9. We cover the lobe $L_{2,1}(1)$ in R2 (and partially in R3) with a uniform grid of points (spacing $= 0.006$) at time $z = 0$, as shown in figure 9(*a*). We when show in figure 9(*b*) that the tracer lies inside R1, exactly in the spiral-shaped turnstile lobe $T_0^{\frac{1}{2}} L_{2,1}(1)$, at time $z = \pi$. In Kaper (1991, figures 2.18*c* and *d*), the shaded region is blown up so that the boundaries of the thin, lamellar striations are clearly visible. Particles only lie in the lobes.

Furthermore, two cases are possible, one in which $L_{2,1}(1) \cap L_{3,2}(1) \neq \emptyset$, as shown in figure 8(*d*), and the other in which $L_{2,1}(1) \cap L_{3,2}(1) = \emptyset$. However, for $\epsilon < 0.3$ in all of the cases we analysed the former holds true. This explains why we said above that $L_{2,1}(1)$ is a subset of R2 and R3. The results we present in the remainder of this paper apply in both cases; one need only be slightly careful about justifying the formulae we use in the former case, as we show in the next section.

### 5.3. *Transport in intervals of unit periods*

In this section, we look at the inter-regional transport process from the usual, per-unit-period point of view and obtain results giving the probability that an orbit initially in one region can be found in another region after any period of the modulation. Rather than treat this problem in its full generality immediately, however, we first consider the particular problem of what fraction of tracer initially in R3 gets transported to R1 in each period of the modulation.

One may then compute the other eight quantities $T_{i,j}(n)$ for $i,j = 1,2,3$, which, assuming that region $i$ is initially filled with tracer fluid, represent the amount of tracer initially in region $i$ that is in region $j$ exactly at the end of the $n$th period. These can be

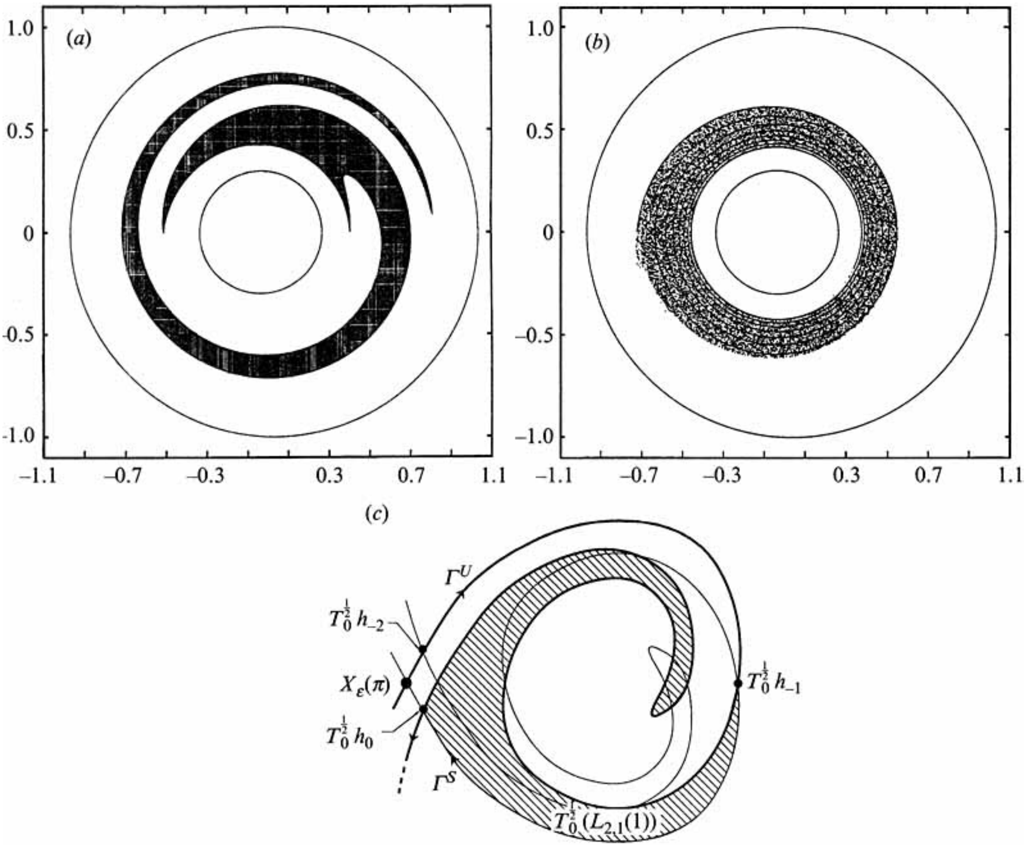

FIGURE 9. Transport in half-period intervals via the turnstile mechanism in the case $\bar{e} = 0.1$, $\bar{r} = 0.3$, $\epsilon = 2\pi/40$, and (MP1). (*a*) All tracer particles at $z = 0$ lie in lobe $L_{2,1}(1)$, which is shaded. (*b*) At $z = \pi$, all tracer particles lie in $T_0^{\frac{1}{2}}(L_{2,1}(1))$ R2, the half-period image of the lobe $L_{2,1}(1)$. Enlargement of (*b*) shows that all of the particles lie inside the half-period image of the lobe, which has a solid boundary. (*c*) Schematic of (*b*).

used to give the probabilities, using the same procedure as we do here for $T_{3,1}(n)$ and the conservation equations. These equations, five in all for the nine independent quantities $T_{i,j}(n)$ for $i,j = 1,2,3$, express the conservation of tracer and the conservation of the areas $\mu(R_i)$ for $i = 1,2,3$:

$$\left.\begin{aligned} \sum_{j=1}^{3}(T_{i,j}(n)-T_{i,j}(n-1)) = 0, \quad i = 1,2,3, \\ \sum_{i=1}^{3}(T_{i,j}(n)-T_{i,j}(n-1)) = 0, \quad j = 1,2,3. \end{aligned}\right\} \tag{5.2}$$

The solution to this problem represents the probability that an orbit, initially rotating in the same sense as the casing, changes flow direction as a function of the modulation period. To define the problem precisely, we assume that the tracer is uniformly concentrated in R3 initially, i.e. at the slow time $z = 0$. The question we answer, then, is: how much tracer is in R1 at time $z = 2n\pi$ for $n = 1,2,\ldots$? We label this quantity as $T_{3,1}(n)$.

Before proceeding, we must redefine the turnstile lobes to eliminate the intra-turnstile overlap areas $L_{1,2}(1) \cap L_{2,1}(1)$ and $L_{2,3}(1) \cap L_{3,2}(1)$. The two lobes forming a turnstile always intersect in adiabatic dynamical systems, due to the lobe area theorem given in Kaper & Wiggins (1991*a*). In particular, we set

$$\left.\begin{aligned}\tilde{L}_{1,2}(1) &\equiv L_{1,2}(1)\bigcap R1,\\ \tilde{L}_{2,1}(1) &\equiv L_{2,1}(1)-L_{2,1}(1)\bigcap L_{1,2}(1),\\ \tilde{L}_{2,3}(1) &\equiv L_{2,3}(1)\bigcap (R2\bigcup R1),\\ \tilde{L}_{3,2}(1) &\equiv L_{3,2}(1)-L_{3,2}(1)\bigcap L_{2,3}(1).\end{aligned}\right\} \tag{5.3}$$

The excluded parts of the original turnstile lobes, although they get mapped across the inter-regional boundaries during the first half of the modulation period, get mapped back across before the end of the period to the region they were in at the beginning of the period. For example, during every period the fluid in $L_{2,1}(1) \cap L_{1,2}(1)$ gets mapped from R2 into R1 and back again. Therefore, the orbits in these overlapping regions change their orbit type (i.e. rotate in the same sense as the shaft or the casing, or are in the instantaneous backflow region) an even number of times in each period, and the parts in the redefined lobes do so an odd number of times.

Now, the fact that $\Gamma^S$ cannot self-intersect implies that $L_{1,2}(1)$ must lie in $L_{2,1}(1)$ and R1, because as soon as it crosses $\Gamma^U$ between $X_\epsilon(z_0)$ and $h_1$ it does so at the pip which defines the boundary of $L_{1,2}(1)$. Thus, the overlap region is large. In fact the turnstile lobes overlap completely in the limit of $\epsilon \rightarrow 0$, as we will see in the next section.

In addition, exclusion of the intra-turnstile overlap, which may be characterized by saying that we exclude, for example, from $L_{2,1}(1)$ the (large) piece of the lobe $L_{1,2}(1)$ 'nested' inside $L_{2,1}(1)$, isolates the long thin folded structure of $\tilde{L}_{2,1}(1)$ that gets transported into R1 at the end of each cycle. We now show that it is responsible for continuing the stretching and folding of the lamellar tracer structure discussed in the previous section as $z$ increases from $z = \pi$ to $z = 2\pi$ and in each subsequent period.

$\tilde{L}_{2,1}(1)$ directly transports an amount of fluid equal to $\mu(\tilde{L}_{2,1}(1) \cap \tilde{L}_{3,2}(1))$ from R3 into R1 during each period, where $\mu(L)$ denotes the area of the planar set $L$. In fact, only the tracer contained in the intersections of $\tilde{L}_{2,1}(1)$ with $T_0^{n-k}\tilde{L}_{3,2}(1)$, for $k = 1, 2, \ldots, n-1, n$, can enter R1 at the $n$th iteration.

However, the intersection $\tilde{L}_{2,1}(1) \cap \tilde{L}_{3,2}(1)$ is only uniformly filled with tracer fluid initially. At later times, the concentration of tracer is not uniform. Furthermore, although the fluid in this and the other intersections is exactly what we need, not all of it is tracer fluid. Thus, the problem requires us not only to identify the flux mechanism, as we have done so far, but also to find a way to determine the content of the lobes.

Having redefined the turnstile lobes, the transport theory presented in Rom-Kedar & Wiggins (1990) directly determines the lobe content. The two main quantities needed are the amount of tracer which is in the lobes $\tilde{L}_{2,1}(n)$ and $\tilde{L}_{1,2}(n)$, which we denote by $\tilde{L}^3_{2,1}(n)$ and $\tilde{L}^3_{1,2}(n)$ following the notation of Rom-Kedar & Wiggins (1990), where the superscript 3 indicates that we are following the tracer which was initially uniformly distributed in R3. For $n > 1$, we find

$$\left.\begin{aligned}\mu(\tilde{L}^3_{2,1}(n)) &= \mu(\tilde{L}_{2,1}(1)\bigcap \tilde{L}_{3,2}(1))\\ &\quad+\sum_{k=1}^{n-1}\{\mu(T_0^{k-n}\tilde{L}_{2,1}(1)\bigcap L_{3,2}(1))-\mu(T_0^{k-n}\tilde{L}_{2,1}(1)\bigcap \tilde{L}_{2,3}(1))\},\\ \mu(\tilde{L}^3_{2,1}(n)) &= \mu(\tilde{L}_{1,2}(1)\bigcap \tilde{L}_{3,2}(1))\\ &\quad+\sum_{k-1}^{n-1}\{\mu(T_0^{k-n}\tilde{L}_{1,2}(1)\bigcap L_{3,2}(1))-\mu(T_0^{k-n}\tilde{L}_{1,2}(1)\bigcap \tilde{L}_{2,3}(1))\}\end{aligned}\right\} \tag{5.4}$$

At first glance it may seem that, in addition to redefining the turnstile lobes as we did above, we also must modify the transport theory, because of the fact that part of $\tilde{L}_{2,1}(1)$ lies in R3 and part of $\tilde{L}_{2,3}(1)$ lies in R1. However, the above formulae are exactly the necessary ones because the intersections with $\tilde{L}_{3,2}(1)$ and $\tilde{L}_{2,3}(1)$ are accounted for from the first period onward.

Next, the change in the amount of tracer in R1 at the $n$th cycle is

$$T_{3,1}(n) - T_{3,1}(n-1) = \mu(\tilde{L}^3_{2,1}(n)) - \mu(\tilde{L}^3_{1,2}(n)). \tag{5.5}$$

Using (5.4), we evaluate the right-hand side. Finally, we write a (telescopically collapsing) sum using the above difference formula to obtain $T_{3,1}(n)$ strictly as a function of $T_{3,1}(0)$ and the lobe content expressions (5.4):

$$T_{3,1}(n) = T_{3,1}(0) + \sum_{m=1}^{n-1} (n-m)\{\mu(\tilde{L}_{2,1}(1) \bigcap T_0^m \tilde{L}_{3,2}(1)) - \mu(\tilde{L}_{2,1}(1) \bigcap T_0^m \tilde{L}_{2,3}(1))\}. \tag{5.6}$$

Since by assumption all of the tracer is in R3 initially, $T_{3,1}(0)$ is identically zero, and (5.6) reduces to

$$T_{3,1}(n) = \sum_{m=1}^{n-1} (n-m)\{\mu(\tilde{L}_{2,1}(1) \bigcap T_0^m \tilde{L}_{3,2}(1)) - \mu(\tilde{L}_{2,1}(1) \bigcap T_0^m \tilde{L}_{2,3}(1))\}. \tag{5.7}$$

### 5.4. *Exponential stretching of material interfaces and lobes*

In this section we use the notion of Birkhoff signatures to analytically obtain exponentially growing lower bounds on the stretching rates for both interfaces and lobes. In addition, we show theoretically that the rate at which a patch of tracer fluid is stretched asymptotes to some constant rate after the first several periods. The numerical data we collected from simulations $O(10^5)$ points in typical case agree with our analytical expressions and are reported in §6. The actual stretching rates predicted by our theory for patches in continuously modulated flows appear to be similar to those reported in Muzzio *et al.* (1991) for blinking flows.

Relying on the invariance of the stable and unstable manifolds, Birkhoff signatures represent a compact way to encode the relevant data about the homoclinic tangles in quasi-steady Stokes flows. We begin by illustrating schematically in figure 10, using a simple example, how the unstable manifold winds around the stable manifold, forming a homoclinic tangle, as the fixed point, $X_\epsilon$, of the Poincaré map is approached. The segments between the principal intersection points $h_0$ and $h_2$ constitute the fundamental pattern, or 'basic signature', which gets repeated at every iteration of the Poincaré map in the following sense. As we stated in §5.1, pips get mapped to pips. In particular, $T_0 h_i = h_{i+2}$ for all integers $i$. As we saw in the previous section, the segments of the stable and unstable manifolds between pip's are mapped to the appropriate segments between the forward images of the pip's under the action of the Poincaré map in such a way that the relative ordering of initial conditions stays the same, due to uniqueness of solutions. Therefore, from the basic signature we can obtain a sequence of signatures which schematically (and topologically) encode the entire tangle.

In this example, as we go from $h_1$ to $h_2$ along $W^U(X_\epsilon(z_0))$, $U[h_1, h_2]$ arches back toward $h_0$ and intersects $S[h_0, h_1]$ in two secondary homoclinic points, $s_1$ and $s_2$. Because $s_1$ and $s_2$ lie on $S[h_0, h_1]$, we know that $s_3 \equiv T_0 s_1$ and $s_4 \equiv T_0 s_2$ are on the segment $S[h_2, h_3]$ and that $U[h_3, h_4]$ intersects $S[h_2, h_3]$ in those two points. Therefore, $U[h_3, h_4]$ must wind around $U[h_1, h_2]$ as sketched in figure 10 because the unstable manifold cannot self-intersect. Following Abraham & Shaw (1985), we refer to the segments of $W^U(X_\epsilon(z_0))$ and $W^S(X_\epsilon(z_0))$ between $h_0$ and $h_4$ as the second signature. This fundamental

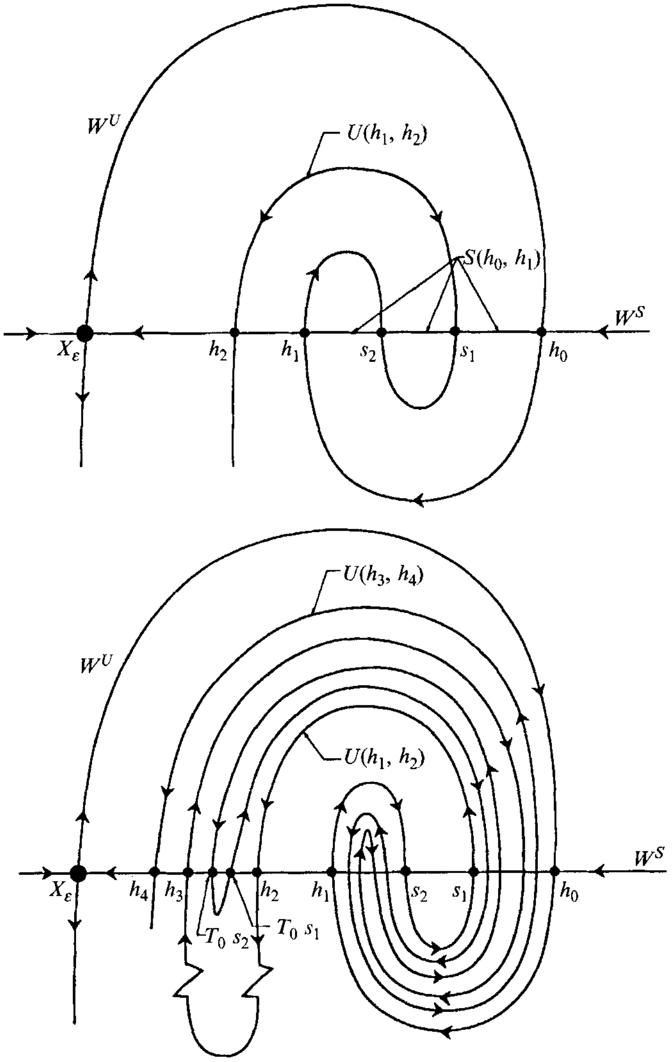

FIGURE 10. Basic and second Birkhoff signatures for the simple example of §5.4.

process, i.e. $U[h_{2i+1}, h_{2i+2}]$ intersecting $S[h_{2i}, h_{2i+1}]$ and winding back to $h_0$ around the previous segments of the unstable manifold (creating higher-order homoclinic points), repeats itself for every $i \geqslant 1$. Furthermore, in this process, the interface is stretched by a factor of at least twice the length of $U[h_1, h_2]$ each iteration because the pieces of the segments which wind back are at least as long as the 'finger' of $U[h_1, h_2]$ arching back. Thus, denoting the length of a segment $U[h_1, h_{1+1}]$ by $l(U(h_1, h_{1+1}])$, we have

$$l(U[h_{2i+1}, h_{2i+2}]) > 2^i l(U[h_1, h_2]), \tag{5.8}$$

for all integers $i$, where this lower bound is conservative, but rigorous.

Using the concepts illustrated on this simple example, we analyse a typical case. For the parameters $\bar{e} = 0.1$, $\bar{r} = 0.3$, $\epsilon = 2\pi/40$, and (MP1), we focus on the tangle formed by $A^S(X_\epsilon(z_0))$ and $A^U(X_\epsilon(z_0))$. The basic signature for this tangle shows that $U[h_1, h_2]$ and $S[h_0, h_1]$ intersect in many more (eighteen, in this case) secondary homoclinic points. Thus, the long length of these segments gets stretched exponentially in time by the above inequality. This also implies that the length of a lobe (a quantity defined

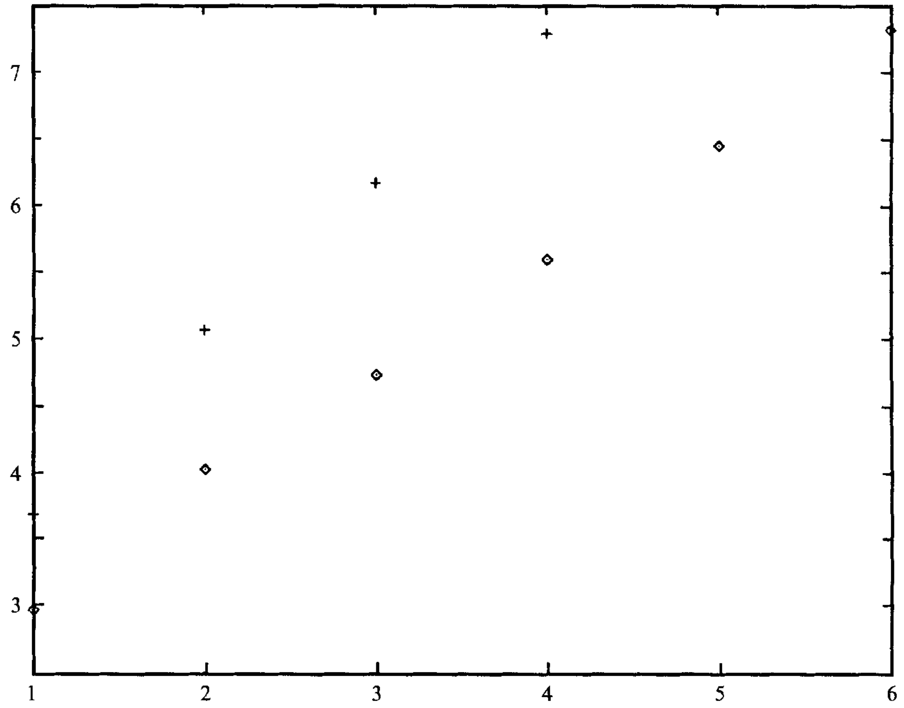

FIGURE 11. Plots of the natural logarithm of the length of the unstable manifold (vertical axis) as a function of the modulation period $n$ (horizontal axis) for two typical cases. In both $\bar{e} = 0.1$, $\bar{r} = 0.3$, and (MP1) were used, and the squares correspond to the case of $\epsilon = 2\pi/20$ and the pluses to $\epsilon = 2\pi/30$. The slopes are very near the stretch rate predicted by the Birkhoff signature analysis, which is the line with slope $\ln 2$. These arclength measurements were made numerically and corroborated using a map wheel.

carefully in the next section) grows exponentially in time. In figure 11, we graph the exponential rate of stretching of the manifold as a function of the modulation period for two typical cases.

## 6. Analytical estimates from adiabatic dynamical systems theory

### 6.1. *Adiabatic Melnikov theory*

The first tool we need is the adiabatic Melnikov function, $M_A(z)$, see Neishtadt (1975), Robinson (1983), Palmer (1986), Wiggins (1988*a–c*), or Kaper & Wiggins (1991*a*). It is the coefficient of the leading-order term in an asymptotic series for the distance between the stable and unstable manifolds forming a 'same pair' tangle as measured along the normal to the instantaneous stagnation streamlines:

$$M_A(z) \equiv \int_{-\infty}^{\infty} t\left(\frac{\partial\psi}{\partial x}\frac{\partial^2\psi}{\partial y\,\partial z} - \frac{\partial\psi}{\partial y}\frac{\partial^2\psi}{\partial x\,\partial z}\right)(x_0^z(t), y_0^z(t); z)\,\mathrm{d}t, \tag{6.1}$$

where $(x_0^z(t), y_0^z(t))$ is an orbit parametrizing the instantaneous stagnation streamline for which the function is being evaluated, either $\Gamma^z$ or $\Lambda^z$. If this integral is evaluated along a homoclinic orbit on $\Gamma^z$, we denote the adiabatic Melnikov function by $M_A^{\Gamma}(z)$, and it measures the distance between $\Gamma^S$ and $\Gamma^U$. Similarly, we write $M_A^{\Lambda}(z)$ when the function is evaluated along an orbit on $\Lambda^z$.

A simple zero of $M_A^\Gamma(z)$ implies that, for $\epsilon$ sufficiently small, $\Gamma^S$ and $\Gamma^U$ intersect each other transversely; likewise for $M_A^\Lambda(z)$ and the manifolds $\Lambda^S$ and $\Lambda^U$. Furthermore, for periodic and quasi-periodic systems, one intersection of the manifolds implies that there are infinitely many others, because, as we stated in the previous section, invariance of the manifolds implies that a point on both manifolds must always be on both manifolds.

The theory presented in Kaper & Wiggins (1991*a*) shows that $M_A^\Gamma(z) = (\mathrm{d}A^\Gamma/\mathrm{d}z)(z, z_0)$, where $A^\Gamma$ is the difference between the areas enclosed by the instantaneous separatrices $\Gamma^z$ and $\Gamma^{z_0}$ and $z_0$ is the zero of $M_A^\Gamma(z)$ corresponding to the nearest intersection and extremal instantaneous separatrix. A similar result holds for $M_A^\Lambda(z)$. Therefore, since $\mathrm{d}A/\mathrm{d}z$ changes sign at the extremal values of $z$, we know that both $M_A^\Gamma(z)$ and $M_A^\Lambda(z)$ have periodically spaced simple zeros for our modulation protocols at $z = 0$, $\pi \bmod 2\pi$, and hence the intersecting stagnation streaklines form two homoclinic tangles as shown in the figures of the previous section. Alternatively, (6.1) may be rewritten in a computationally more convenient manner, as is shown in Kaper & Wiggins (1991*a*), as

$$M_A^\Gamma(z) = \int_{-\infty}^{\infty} \left( \frac{\partial \psi}{\partial z}(\Gamma(z), z) - \frac{\partial \psi}{\partial z}(X_0^z, z) \right) \mathrm{d}t. \tag{6.2}$$

Using this form, one can also see that the adiabatic Melnikov functions for both separatrices have simple zeros at $z = 0$, $\pi \bmod 2\pi$, because the derivative on $\psi$ only contains terms proportional to $\sin z$ and hence vanishes there. Thus, we have rigorously established the existence of the intersections of the manifolds we obtained numerically in the previous section.

Furthermore, the theory of the adiabatic Melnikov function enables us to show that all of the pips $h_i$ and $k_t$, for all integers $i$, except $i = 0$, lie in a small neighbourhood $\mathcal{N}_\epsilon$, whose size depends on $\epsilon$, of $X_\epsilon(z)$ on the Poincaré section. Since the $z$-distance between adjacent zeros of both $M_A^\Gamma(z)$ and $M_Z^\Lambda(z)$ is equal to $\pi$, we know that in the fast time $t$, two adjacent pips are separated from each other by a time of flight of $\Delta t = \pi/\epsilon$ along $\Gamma^z$ and $\Lambda^z$, respectively. Thus, on the Poincaré section with $z = 0$, all of the pips $h_i$ and $k_t$, except $h_0$ and $k_0$ which lie near the respective reference points on $\Gamma^z$ and $\Lambda^z$, lie exponentially close in time to $X_\epsilon(z)$ and, hence, in $\mathcal{N}_\epsilon$. This, in turn, implies that the tangles are as shown in the figures from the previous section and that they are very difficult to obtain accurately numerically. Even for values of $\epsilon$ as large as $\epsilon = 2\pi/20$, the time of flight is large enough so that all of the pips but $h_0$ and $k_0$ lie in $\mathcal{N}_\epsilon$. Also, the manifolds are making room for the growing regular zone, which is made up of an increasingly larger number of persistent Arnol'd tori as $\epsilon \to 0$, in the instantaneous backflow region.

### 6.2. *Lobe area*

The lobe area formula established in Kaper & Wiggins (1991*a*, *b*) states that the area of a lobe is given to leading order by the difference between the areas enclosed by the maximum and minimum instantaneous stagnation streamlines that occur during the modulation period. Thus, to leading order the area is an $O(1)$ quantity as $\epsilon \to 0$, which is strikingly different from the regular perturbation case in which the leading-order term is $O(\delta)$ asymptotically. Furthermore, in Kaper & Wiggins (1991*b*), we have shown that the remaining terms in the asymptotic expansion are $O(\epsilon)$.

The data required to determine the $O(1)$ contributions to the lobe areas for our flows may be read from the tables given in §2. To be precise, the leading-order term in the asymptotic expansion for the area of $L_{2,1}(1)$ and all of the other lobes in the $\Gamma$-tangle

| $\epsilon$ | Length | Average width |
|---|---|---|
| $2\pi/30$ | 3.93 | 0.15 |
| $2\pi/40$ | 5.65 | 0.11 |
| $2\pi/50$ | 8.31 | 0.079 |
| $2\pi/60$ | 11.06 | 0.061 |

TABLE 4. Lobe length and average width for the turnstile lobe $L_{21}(1)$ as a function of $\epsilon$. (MP1) is used, $\bar{e} = 0.1$, and $\bar{r} = 0.3$.

(i.e. the tangle formed by the transverse intersections of $\Gamma^S$ and $\Gamma^U$) is the difference between the maximum and minimum areas of region A attained during the given protocol, see table 1. Similarly, the leading-order term in the asymptotic expansion for the area of $L_{3,2}(1)$ and all of the other lobes in the $\varLambda$-tangle is the difference between the maximum and minimum areas of region C attained during the given protocol, see table 1.

Finally, the integral of $M_A(z)$ between two of its adjacent simple zeros gives the same result as the leading-order term for the lobe area, see Kaper & Wiggins (1991*a*). We have used this property to verify the correctness of our computations. For all of the geometries and protocols we simulated, the lobe-area results scale according to the theory.

### 6.3. *Length of turnstile lobes*

Given that we know the lobe area, we now determine the shape of the first turnstile lobes and then those of all of their images. Independently of our lobe-area result, but essential in their own derivation of that result, Elskens & Escande (1991) stated a result for the lengths of turnstile lobes which, in the context of our flows, implies that the lengths of the two turnstile lobes $L_{2,1}(1)$ and $L_{3,2}(1)$ are $O(1/\epsilon)$ as $\epsilon \rightarrow 0$ to leading order. Here, we measure the length from the midpoint of the base segment, $U[X_\epsilon(z), h_0]$ and $U[X_\epsilon(z), k_0]$, respectively, of the lobe to its 'tip', see figure 8(*a*). Our measurement is the number (including the fractional part) of times the lobe spirals around in the fluid domain multiplied by the average length of one spiral. As may be seen by uncoiling the lobe, our measurement constitutes the analogue of Elskens & Escande's measurement of lobe length using the distance from the base to the tip of the lobe along the $q$-axis in the pendulum. The asymptotic scaling depends on $\epsilon$, and the coefficients in the expansion depend on $\bar{e}$ and the choice of protocol through $\Delta\bar{\Omega}$.

Since our $O(1)$ lobe-area result given in the previous subsection is independent of this length calculation, we know that the average width of the lobe is $O(\epsilon)$, as measured along the normal to the segments of $\Gamma^S$ and $\varLambda^S$ that define it. We report the lengths and average widths of the lobes $L_{2,1}(1)$ and $L_{3,2}(1)$ for different cases in table 4. We find that the asymptotic scaling is as predicted in the theory. Furthermore, the data from our numerical simulations show that these formulae are fairly accurate for a wide range of small $\epsilon$, up to $\epsilon = 0.34$ in all cases.

### 6.4. *Average striation thickness*

Quantitatively, adiabatic dynamical systems theory predicts that a patch of tracer fluid gets stretched by a factor of $O(1/\epsilon)$ in each period of the modulation. Also, in §5.4, we have shown that the unstable manifold forming the boundary of the lobes grows exponentially in length. Thus, we may estimate that the average striation thickness, which is approximately the average width of the lobes, decreases with time as follows:

$$d_{\text{striation}}(z = 2n\pi + z_0; t = 2n\pi/\epsilon) = O(\epsilon/2^n) \tag{6.3}$$

| $\epsilon$ | Period | $d_{\text{striation}}$ | No. folds |
|---|---|---|---|
| $2\pi/20$ | 1 | $2.1 \times 10^{-3}$ | 4 |
| $2\pi/20$ | 2 | $7.1 \times 10^{-4}$ | $23 \pm 2$ |
| $2\pi/20$ | 3 | $3.5 \times 10^{-4}$ | $72 \pm 7$ |
| $2\pi/20$ | 4 | $1.5 \times 10^{-4}$ | $180 \pm 15$ |
| $2\pi/20$ | 5 | $6.3 \times 10^{-5}$ | — |
| $2\pi/20$ | 6 | $2.7 \times 10^{-5}$ | — |
| $2\pi/30$ | 1 | $1.2 \times 10^{-3}$ | 16 |
| $2\pi/30$ | 2 | $3.9 \times 10^{-4}$ | $63 \pm 3$ |
| $2\pi/30$ | 3 | $8.0 \times 10^{-5}$ | $168 \pm 7$ |

TABLE 5. Average width of tracer patch and number of folds in the patch as a function of $\epsilon$ and the modulation period. Folds are defined as bends in the patch with an angle of more than 90°. Data for the fifth and sixth periods are not reported because of the difficulty in finding their number using simulations with 20000 points. (MP1) is used, $\bar{e} = 0.1$, and $\bar{r} = 0.3$.

for integer $n$. Table 5 contains the data for the average striation thickness and the number of folds as a function of the modulation period from various simulations.

The evolution of an arbitrary patch of tracer fluid in the mixing zone is determined completely by the evolution of the set of lobes it is in. Any part of the patch in a turnstile lobe gets stretched, folded, and 'thinned' by the same amount as the lobe. The same applies to those parts of the patch which are in other lobes, outside of the turnstile lobes.

## 7. Analytical determination of island location and size

Islands are invariant regions in which fluid particles advect in a regular (integrable) sense. They obstruct transport since fluid cannot leave or enter them. In this section, we apply new results to obtain information about the location and size of islands. As an example to illustrate the further control we have over the flow domain using our modulation protocols, we show how one can choose the frequency of modulation so that one minimizes the area in the mixing zone occupied by islands and hence maximizes the area in which exponential stretching occurs. Islands are distinct from regular zones, even though they look exactly like regular zones, since they are made up of tori created around elliptic periodic points. However, islands surround elliptic points which are created in global bifurcations as resonant responses to the time-periodic modulation. They are not made up of tori which persist from the steady-state flow. Thus they are different from the tori which make up regular zones. The results of Kaper (1991, Part I) and those of Elskens & Escande (1991) show that these islands are no bigger than $O(\epsilon)$. All of the numerical simulations we performed with $\epsilon < 0.2$ are consistent with these results.

From a typical plot, see figure 12, of the periods of the steady-state orbits versus the point at which they intersect the $x$-axis in the wide part of the annular gap in the bearing, one sees that the period diverges logarithmically to infinity as the stagnation streamlines $\Gamma^z$ and $\Lambda^z$ are approached. The orbital frequency is given by $2\pi$ divided by the period, so it vanishes logarithmically near the separatrices. Finally, the modulation frequency satisfies $0 < \epsilon \ll 1$. As a consequence, the orbits which resonate with the modulation, i.e. those whose natural frequency is some rational multiple of $\epsilon$, spend most of the modulation period very close to the slowly moving saddle stagnation points, and only near distinguished values of the slow time ($z = 0, \pi \bmod 2\pi$) do they

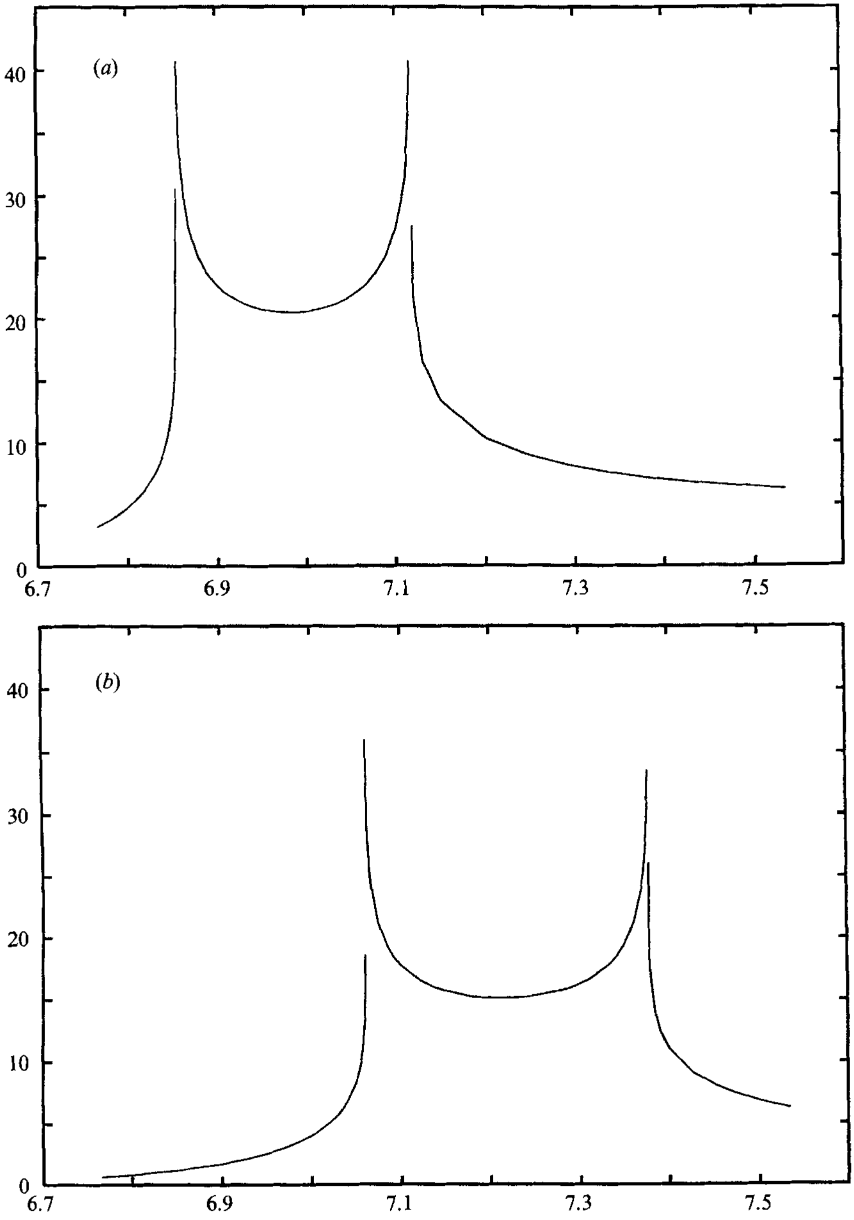

FIGURE 12. The period (in radians on the vertical axis) of the steady-state periodic orbits versus the position ($x$) of the orbit along the wide gap between the shaft and the casing. $\bar{e} = 0.1$, $\bar{r} = 0.3$, $\Omega_1 = 1.0$; in (a) $\Omega_2 = -2$ and in (b) $\Omega_2 = -10$. The inner and outer cylinders are at $x = 6.765$ and $x = 7.535$, respectively. The period goes to infinity logarithmically as $\Gamma$ and $\Lambda$ are approached.

make excursions away from it near the instantaneous stagnation streamlines. Matched asymptotic expansions can be constructed for the resonant subharmonics.

Finally, the islands are created in global bifurcations. In the case of $\bar{e} = 0.1$, $\bar{r} = 0.3$, (MP1), there is a global bifurcation between $\epsilon = 2\pi/20$ and $\epsilon = 2\pi/30$ in which the intersection point $h_0$ of the manifolds $\Gamma^S$ and $\Gamma^U$ is created. This event is correlated with the fact that just below $\epsilon = 2\pi/20$, the period of the modulation (period = 20 in the units in figure 12) first exceeds the minimum period of orbits in the backflow region;

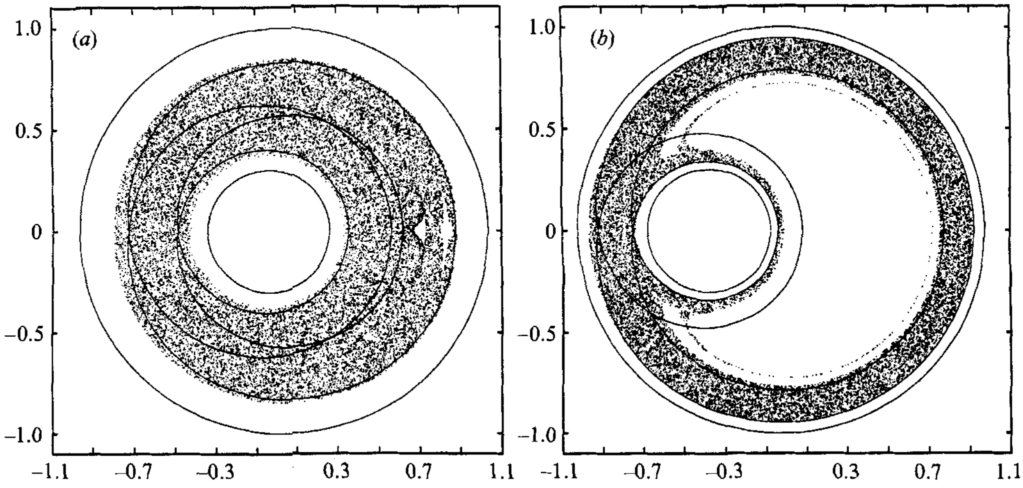

FIGURE 13. Actual mixing zone for (*a*) $\bar{e} = 0.1$, $\bar{r} = 0.3$, $\epsilon = 2\pi/20$, with (MP1); and (*b*) $\bar{e} = 0.5$, $\bar{r} = 0.3$, $\epsilon = 2\pi/60$, with (MP1). In both cases, one initial condition is integrated for 20000 periods.

recall that $\Omega_2 = -2$ at $z = 0 \bmod 2\pi$. Now, for this same case, we first see the (small) 2:1 island when $\epsilon$ reaches $2\pi/20$, see figure 13(*a*).

Also, these results are asymptotic. For example the 1:1 island in the case for which $\bar{e} = 0.5$ and (MP1) are used is big for $\epsilon$ as small as $2\pi/60$, see figure 13(*b*). Again, there is a global bifurcation below this value of $\epsilon$ in which, as $\epsilon$ decreases, a new homoclinic point is created.

## 8. Chaotic fluid particle motion

Although chaos is not the primary focus of our study we state briefly in what sense these slowly modulated counter-rotating flows exhibit chaotic dynamics. Since the flow in the counter-rotating eccentric journal bearing subject to the modulation protocols (MP1) and (MP2) has two intertwined homoclinic tangles, the Smale–Birkhoff Homoclinic Theorem directly implies that horseshoes exist. Among the possible horseshoe constructions, the main two are the 'same pair' horseshoes created by each of the tangles individually, i.e. $\Gamma^S(X_\epsilon(z_0))$ with $\Gamma^U(X_\epsilon(z_0))$ or $\Lambda^S(X_\epsilon(z_0))$ with $\Lambda^U(X_\epsilon(z_0))$, and the 'mixed pair' horseshoes formed by the transverse intersections of 'mixed pairs' of manifolds, i.e. $\Gamma^S(X_\epsilon(z_0))$ with $\Lambda^U(X_\epsilon(z_0))$ or $\Lambda^S(X_\epsilon(z_0))$ with $\Gamma^U(X_\epsilon(z_0))$. Also, the theory of adiabatic dynamical systems, see Kaper & Wiggins (1991*c*), implies that these flows possess the basic stretching and folding required so that the horseshoe construction can occur in one iteration of the Poincaré map, just as 'whorl-tendril' flows do (see Ottino 1989).

## 9. Robustness of the model

### 9.1. *Incorporation of inertial effects*

In our model, we assume that the flow is determined exactly by the solution of the Stokes equations. Incorporation of inertial effects does not alter either the essential features of the streamline pattern from those of our model or the leading-order results obtained from the analysis presented in previous sections.

The essential features of the steady counter-rotating flow are the saddle stagnation point, the two streamlines which stagnate on it, and the three families of periodic streamlines bounded by them. For $0 < Re \ll 1$, the position of the saddle and the two stagnation streamlines changes by an amount of $O(Re)$ from that which we used in the Stokes model. The expansion for the position of the saddle taking into account the first-order inertial terms performed in Ballal & Rivlin (1976) shows that the $y$-component of its position changes by an $O(Re)$ amount whereas the $x$-component is unaltered from that of $X_0^{z_0}$. Furthermore, the saddle is still connected to itself by two stagnation streamlines (slightly tilted from the position of $\Gamma^{z_0}$ and $\Lambda^{z_0}$) which are level curves of the enhanced stream function, i.e. the stream function obtained when the first correction terms for inertia are included, see Ballal & Rivlin (1976, figure 26).

Robustness of the streamline pattern is one of the main reasons we chose the counter-rotating case. The flow in the corotating case is more delicate. If $\bar{\Omega} > \bar{\Omega}_{\mathrm{crit}} > 0$, there exist two saddle stagnation points in the corotating case connected to each other by four stagnation streamlines (heteroclinic orbits), see Ballal & Rivlin (1976, figure 14). Although addition of the inertial effects only changes the locations of these two saddle points by an amount of $O(Re)$ (just as in the counter-rotating case), the topography of the level curves of the full stream function is changed. See, Ballal & Rivlin (1976, figure 22) for comparison. In particular, the value of the enhanced stream function is no longer the same at the two stagnation points so that they cannot be connected to each other as they are in the $Re = 0$ limit. Instead of having four heteroclinic orbits, one has two homoclinic orbits, one to each saddle. Thus, although the time-periodic modulation will make the corotating flow exhibit good mixing because the two homoclinic orbits break and sweep out a large area, one cannot apply the results from the $Re = 0$ model to the full flow and one needs to perform a detailed analysis based on the enhanced stream function instead.

However, since there are two slowly moving saddle points when $\bar{\Omega} > \bar{\Omega}_{\mathrm{crit}}$ which stretch material elements in the corotating case, as opposed to only one in the counter-rotating case, mixing may be more efficient.

Finally, when one of the cylinders remains stationary, the position of the stagnation point on the stationary cylinder depends only on the eccentricity of the bearing and is independent of the angular velocity of the spinning cylinder, at least at the level of the Stokes approximation (see Ballal & Rivlin 1976). Since the inertial corrections are $O(Re)$, the maximum area that the stagnation streamlines could sweep out and, hence, the maximal area available for mixing in the context of continuous modulation protocols, is much smaller than it can be in the counter-rotating or corotating cases.

### 9.2. *Application to other mixing problems*

The techniques that we have presented may be applied to a large class of quasi-steady Stokes flows with features commonly found in adiabatic dynamical systems.

Large-scale chaos exists in the blinking two-roll mill, see for example Ng (1989) and Ng, James & Leal (1990). In this device, there are two cylinders external to each other in a box. Using modulation protocols such as those in §3, the angular velocities of the two cylinders are functions of the slow time $z$. An interesting case is when the saddle stagnation point moves slowly back and forth along the gap between the two cylinders, see Kaper & Wiggins (1989). Large $O(1)$ chaotic regions are created just as they are in the eccentric journal bearing flow because the saddle and its stable and unstable manifolds sweep out $O(1)$ distances. Furthermore, all of the techniques discussed in the previous sections can be applied directly to extract quantitative information.

In addition, our method may be applied to systems for which the stream function is not known. One needs to look at a sequence of steady-state flows and find a saddle stagnation point attached to itself or other points by a stagnation streamline for each flow in the sequence. If the position of that stagnation streamline changes over an $O(1)$ distance in this family of steady states, then one can modulate the flow in time as we do, and the leading-order terms for the transport quantities may be obtained directly from measurements of the steady-state flows at the instants of time corresponding to the peaks and valleys of the modulation protocol. These measurements can be made, for example, from photographic or digitized images of the steady-state flow. Thus, in the case of some cavity flow or geophysical applications (Hoffman & McKenzie 1985), in which the stream function is often not known or known only approximately, further analytical results are possible.

It may even be possible to get mixing when the saddle stagnation point disappears for part of the modulation period, although this does not appear to be as efficient as the cases considered here. Coppola & Rand (1991) give a mechanical example of such an adiabatic Hamiltonian system. Also, no analytic techniques, such as KAM theory or Melnikov theory, exist to handle this class of problems.

### 9.3. *Molecular diffusion*

In the foregoing sections, we have restricted ourselves to simulating the ideal case in which the transport of tracer particles in the quasi-steady Stokes flow occurs only via convection. We now make our study more realistic and consider also the impact of molecular diffusion in the transport process. Our results show that diffusion of tracer particles is important from the beginning of any experiment and has a macroscopic impact on the location of convectively transported tracer particles.

In the simulations, we model the effects of molecular diffusivity by adding a term representing the Brownian motion that a tracer particle experiences due to molecular diffusivity to the characteristic equations (the purely convective model) of the partial differential equation governing the advection and diffusion of tracer concentration. In particular, we use a generalized Langevin equation:

$$\left.\begin{aligned} \dot{x} &= \frac{\partial \psi}{\partial y}(x,y;\Omega_1(z),\Omega_2(z))+\zeta_1(t), \\ \dot{y} &= -\frac{\partial \psi}{\partial x}(x,y;\Omega_1(z),\Omega_2(z))+\zeta_2(t), \\ \dot{z} &= \epsilon, \end{aligned}\right\} \tag{9.1}$$

where $\psi$ is the stream function used in the purely convective simulations, and $\zeta_i(t)$, $i=1,2$, are random variables drawn from a Gaussian probability distribution characterized by the following correlations:

$$\left.\begin{aligned} \langle \zeta_i(t)\,\zeta_i(t')\rangle &= 2D\delta(t-t'), \\ \langle \zeta_i(t)\,\zeta_j(t')\rangle &= 0. \end{aligned}\right\} \tag{9.2}$$

for $i,j=1,2$ and $i \neq j$. See Chandrasekhar (1943) for the theory of Brownian motion, and Dutta & Chevray (1991) for another study of diffusive effects in chaotic Stokes flows.

The amount by which patches are stretched is somewhat enhanced due to diffusion. In particular, the locations of the 'tips' of patches are changed by amounts on the order of $5\% \pm 2\%$ of the length of the spiral-shaped patch for $D=10^{-8}$ in the first period alone. This percentage was smaller for $D=10^{-9}$ and larger for $D=10^{-7}$. Although an effect of small magnitude may seem insignificant at first glance, it is enhanced in subsequent periods because, as time goes on, convection will also stretch these extra pieces of the deformed patch exponentially.

Furthermore, most of the boundary of a deformed patch remains almost as sharp as it was in the purely convective case. Taking into account that each data point in our numerical simulations represents an infinitesimal area element that gets stretched during the modulation, we find that the deformed patch is narrower on average by an amount that is less than 1% of the convectively stretched patch when $D = 10^{-8}$. The exceptions to this finding are the pieces of the boundary near the 'tips' of the patch, which become fuzzier than they are in the purely convective model.

We thank Tony Leonard for his input and criticisms during various stages of this work. We also thank Gary Leal for many discussions about Stokes flow in the two-roll mill apparatus, and Ricky Ng for consultations concerning connections between experiments. Finally, but not least, we thank the anonymous referees for their careful reading and their many suggestions on improving the presentation of this material. This work has been supported by an ONR Young Investigator Award and an NSF PYI award.

## REFERENCES

ABRAHAM, R. H. & SHAW, C. D. 1985 *Dynamics – The Geometry of Behavior*. Santa Cruz: Ariel.

AREF, H. & BALACHANDAR, S. 1986 Chaotic advection in a Stokes flow. *Phys. Fluids* **29**, 3515–3521.

AREF, H. & JONES, S. 1989 Enhanced separation of diffusing particles by chaotic advection. *Phys. Fluids* A **1**, 470–474.

ARNOL'D, V. I., NEISHTADT, A. I. & KOZLOV, X. (eds.) 1988 *Dynamical Systems*, vol. III, *Encyclopaedia of Mathematical Science*. Springer.

BALLAL, B. Y. & RIVLIN, R. S. 1976 Flow of a Newtonian fluid between eccentric rotating cylinders: inertial effects. *Arch. Rat. Mech. Anal.* **62**, 237–294.

BATCHELOR, G. K. 1967 *An Introduction to Fluid Dynamics*. Cambridge University Press.

BRUHWILER, D. L. & CARY, J. R. 1989 Diffusion of particles in a slowly-modulated wave. *Physica D* **40**, 265–282.

CARY, J. R., ESCANDE, D. F. & TENNYSON, J. 1986 Adiabatic invariant change due to separatrix crossing. *Phys. Rev.* A **34**, 4256–4275.

CARY, J. R. & SKODJE, R. T. 1989 Phase change between separatrix crossings. *Physica D* **39**, 287.

CHAIKEN, J., CHEVRAY, R., TABOR, M. & TAN, Q. M. 1986 Experimental study of lagrangian turbulence in a Stokes flow. *Proc. R. Soc. Lond.* A **408**, 165–174.

CHAIKEN, J., CHU, C. K., TABOR, M. & TAN, Q. M. 1987 Lagrangian turbulence and spatial complexity in a Stokes flow. *Phys. Fluids* **30**, 687–699.

CHANDRASEKHAR, S. 1943 Stochastic problems in physics and astronomy. *Rev. Mod. Phys.* **15**, 1–89.

CHIEN, W.-L., RISING, H. & OTTINO, J. M. 1986 Laminar mixing and chaotic mixing in several cavity flows. *J. Fluid Mech.* **170**, 355–377.

COPPOLA, V. T. & RAND, R. H. 1991 Chaos in a system with a periodically disappearing separatrix. *Nonlinear Dyn.* **1**, 401–420.

DUTTA, P. & CHEVRAY, R. 1991 Effect of diffusion on chaotic advection in Stokes flow. *Phys. Fluids* A 3, 1440.

ELSKENS, Y. & ESCANDE, D. 1991 Slowly pulsating separatrices sweep homoclinic tangles where islands must be small: an extension of classical adiabatic theory. *Nonlinearity* 4, 615.

FRANJIONE, J. G., LEONG, C. W. & OTTINO, J. M. 1989 Symmetries within chaos: a route to effective mixing. *Phys. Fluids* A **1**, 1772–1783.

FRANJIONE, J. G. & OTTINO, J. M. 1987 Feasibility of numerical tracking of material lines in chaotic flows. *Phys. Fluids* **30**, 3641–3643.

GHOSH, S., CHANG, H.-C. & SEN, M. 1991 Heat transfer enhancement due to slender recirculation and chaotic transport between counter-rotating eccentric cylinders, preprint.

GUCKENHEIMER, J. & HOLMES, P. 1983 *Nonlinear Oscillations, Dynamical Systems, and Bifurcations of Vector Fields*. Springer.

HOFFMAN, N. R. A. & MCKENZIE, D. P. 1985 The destruction of geochemical heterogeneities by differential fluid motions during mantle convection. *Geophys. J. R. Astron. Soc.* **82**, 163–206.

KAPER, T. J. 1991 Part I: On the structure in separatrix-swept regions of slowly-modulated Hamiltonian systems; Part II: On the quantification of mixing in chaotic Stokes flows: the eccentric journal bearing. Ph.D. thesis, California Institute of Technology.

KAPER, T. J., & KOVACIC, G. & WIGGINS, S. 1990 Melnikov functions, action, and lobe area in Hamiltonian systems. *Tech. Rep.* LAUR 90-2455 , Los Alamos National Lab.

KAPER, T. J. & WIGGINS, S. 1989 Transport, mixing, and stretching in a chaotic Stokes flow: the two-roll mill. *Los Alamos Tech. Rep.* LA-UR 90-2638; also in *Proc. Third Annual Joint ASCE/ASME Mechanics Conf., La Jolla, July, 1989.*

KAPER, T. J. & WIGGINS, S. 1991*a* Lobe area in adiabatic Hamiltonian systems. *Physica D* **51**, 205–212.

KAPER, T. J. & WIGGINS, S. 1991*b* On the structure of separatrix-swept regions in singularly-perturbed Hamiltonian systems, *Diffl Integral Equat.* **5**, 1363–1381.

KAPER, T. J. & WIGGINS, S. 1991*c* A commentary 'On the periodic solutions of a forced second-order equation' by S. P. Hastings and J. B. McLeod. *J. Nonlin. Sci.* **1**, 247–253

KRUSKAL, M. 1962 Asymptotic theory of Hamiltonian and other systems with all solutions nearly periodic. *J. Math. Phys.* **3**, 806–828.

LEONG, C. W. & OTTINO, J. M. 1989 Experiments on mixing due to chaotic advection in a cavity. *J. Fluid Mech.* **209**, 463–499.

MUZZIO, F. J., OTTINO, J. M. & SWANSON, P. D. 1991 The statistics of stretching and stirring in chaotic flows. *Phys. Fluids* A **3**, 822–834.

NEISHTADT, A. I. 1975 Passage through a separatrix in a resonance problem with a slowly-varying parameter. *Prikl. Mat. Mecl* **39**, 594–605.

NEISHTADT, A. I., CHAIKOVSKII, D. K., CHERNIKOV, A. A. 1991 Adiabatic chaos and particle diffusion. *Sov. Phys. JETP* **72**, 423–430.

NG, R. C.-Y. 1989 Semi-dilute polymer solutions in strong flows. Part I: Birefringence and flow modification in extensional flows; Part II Chaotic mixing in time-periodic flows. Ph.D. thesis, California Institute of Technology.

NG, R. C.-Y., JAMES, D. F. & LEAL, L. G. 1990 Chaotic mixing and transport in a two-dimensional time-periodic Stokes flow – the blinking two-roll mill, in preparation.

OTTINO, J. M. 1989 *The Kinematics of Mixing: Stretching, Chaos and Transport.* Cambridge University Press.

PALMER, K. 1986 Transversal heteroclinic points and Cherry's example of a nonintegrable Hamiltonian system. *J. Diffl Equat.* **65**, 321–360.

ROBINSON, C. 1983 Sustained resonance for a nonlinear system with slowly-varying coefficients. *SIAM J. Math. Anal.* **14**, 847–860.

ROM-KEDAR, V., LEONARD, A. & WIGGINS, S. 1990 An analytical study of the transport, mixing and chaos in an unsteady vortical flow. *J. Fluid Mech.* **214**, 347–394.

ROM-KEDAR, V. & WIGGINS, S. 1990 Transport in two-dimensional maps. *Arch. Rat. Mech. Anal.* **109**, 239–298.

SWANSON, P. D. 1991 Regular and chaotic mixing of viscous fluids in eccentric rotating cylinders. Ph.D. thesis, University of Massachusetts, Amherst.

SWANSON, P. D. & OTTINO, J. M. 1990 A comparative computational and experimental study of chaotic mixing in viscous fluids. *J. Fluid Mech.* **213**, 227–249.

WIGGINS, S. 1988*a* *Global Bifurcations and Chaos: Analytical Methods*, 1st edn. Springer.

WIGGINS, S. 1988*b* On the detection and dynamical consequences of orbits homoclinic to hyperbolic periodic orbits and normally hyperbolic invariant tori in a class of ordinary differential equations. *SIAM J. Appl. Maths* **48**, 262–285.

WIGGINS, S. 1988*c* Adiabatic chaos. *Phys. Lett.* A **128**, 339–342.

WIGGINS, S. 1992 *Chaotic Transport in Dynamical Systems*, 1st edn. Springer.